Journal of Power Sources 667 (2026) 239229

Contents lists available at ScienceDirect

Journal of Power Sources

journal homepage: www.elsevier.com/locate/jpowsour

In-situ grown $Co_{0.5}Ni_{0.5}Se_2$@Nickel-Iron layered double hydroxide heterostructure on nickel foam for high-performance bifunctional electrocatalysis in alkaline and seawater electrolysis

Shuang-shuang Zhang [a], Yong-qi Tian [a], Bo-yao Zhang [a], Yu-wen Pan [a], Yi-bo Wang [a], Jun Xiang [a], De-peng Zhao [b], Rong-da Zhao [a,*], Fu-fa Wu [c,**], Li-hua Miao [d,***]

[a] School of Materials Science and Engineering, Liaoning University of Technology, Jinzhou, Liaoning, 121000, PR China
[b] School of New Energy, Shenyang Institute of Engineering, Shenyang, Liaoning, 110136, PR China
[c] Liaoning Technical University, Fuxin, Liaoning, 123000, PR China
[d] School of Medical Information Engineering, Shenyang Medical College, Shenyang, Liaoning, 110034, PR China

HIGHLIGHTS

- 3D $Co_{0.5}Ni_{0.5}Se_2$@NiFe-LDH: nanowire arrays are directly grown on the surface of Ni foam.
- In 1 M KOH, the catalyst shows the an excellent OER and HER performance.
- In 1 M KOH + seawater, the catalyst shows low overpotential.

GRAPHICAL ABSTRACT

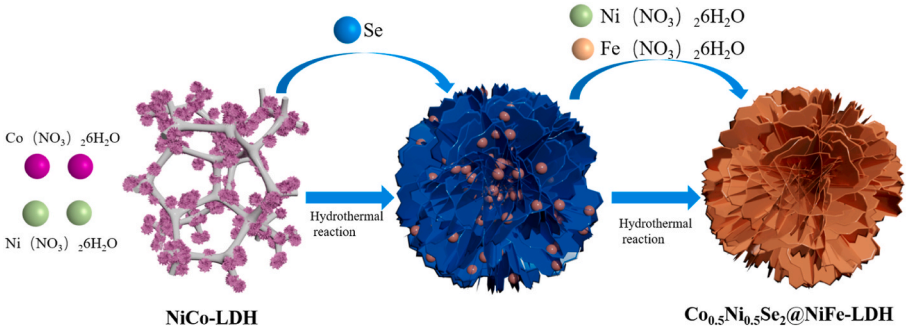

ARTICLE INFO

Keywords:
Hydrogen production via water electrolysis
Heterostructure
Transition metal selenide
Layered double hydroxide (LDH)
Seawater electrolysis

ABSTRACT

Given the pressing global energy crisis, developing high-performance, stable electrocatalysts for hydrogen production through water electrolysis is of paramount significance. In this work, a nickel-cobalt (Ni-Co) precursor is first synthesized on a nickel foam (NF) substrate via a hydrothermal approach, the layered structure of the precursor enables the atomic-scale dispersion of Co^{2+} and Ni^{2+} ions, ensuring that the two metal elements are uniformly distributed in the selenide at a 1:1 ratio after subsequent selenization. Additionally, it can act as a template to guide the selenization and composite reactions, allowing the final product to retain a certain layered derived structure. followed by the in-situ growth of a $Co_{0.5}Ni_{0.5}Se_2$@NiFe-LDH(Nickel-Iron Layered Double Hydroxide) heterostructured catalyst on its surface. Electrochemical tests in a 1 M KOH electrolyte reveal that the as-prepared catalyst exhibits exceptional hydrogen evolution reaction (HER) and oxygen evolution reaction (OER) activities: at a current density of 50 mA cm^{-2}, the required overpotentials are merely 219 mV and 247 mV, respectively. More notably, when tested in an alkaline seawater electrolysis system-an environment closer to

* Corresponding author.
** Corresponding author.
*** Corresponding author.
E-mail addresses: Rongdazhaoln@126.com (R.-d. Zhao), ffwu@lnut.edu.cn (F.-f. Wu), miaolihua@163.com (L.-h. Miao).

https://doi.org/10.1016/j.jpowsour.2025.239229
Received 11 October 2025; Received in revised form 23 December 2025; Accepted 29 December 2025
Available online 2 January 2026

practical application scenarios-the catalyst retains its high catalytic efficiency, with the HER and OER overpotentials increasing only slightly to 223 mV and 249 mV (at 50 mA cm^{-2}). These results underscore the catalyst's promising potential for real-world applications and provide a novel strategy for the design of high-efficiency bifunctional electrocatalysts for water electrolysis.

1. Introduction

In recent years, with the massive and rapid consumption of fossil fuels, global climate change and the energy crisis have attracted increasing attention. Hydrogen, regarded as a promising alternative energy source, can meet our demands for future fuels [1,2]. Electrochemical water splitting converts electrical energy into chemical energy, providing an effective method for producing high-purity hydrogen. However, its practical application is limited by high cost and low efficiency. The presence of electrocatalysts on the cathode and anode electrodes can largely reduce the overpotentials of HER and OER, and promote charge transfer between electrodes as well as between electrodes and electrolytes [3–5]. Currently, the most efficient HER and OER catalysts are noble metals [6–10]. Nevertheless, the scarcity and high price of noble metals severely restrict their large-scale applications [11–13]. Therefore, developing low-cost and high-efficiency non-noble metal electrocatalysts for HER and OER is an urgent priority.

Transition metal-based compounds, such as transition metal oxides [14], hydroxides [15], sulfides [16], phosphides [17], nitrides [18,19], and selenides [20,21], have exhibited excellent electrocatalytic performance in HER and OER. The specific surface area of catalysts can be effectively increased by adjusting their morphology. Doping non-noble metals such as Co and Ni can regulate the electronic structure and conductivity of the catalyst's active centers, thereby enhancing the performance of electrocatalysts [22–25]. The groups of Lv [26] and Lin [27] prepared unique catalysts with sculpturable hollow nanocubes and pea pod-like morphologies, which improved the catalytic performance. Zhang [28] et al. synthesized $NiSe_2$ nanospherical catalysts via a hydrothermal method, which showed high performance both in 1 M KOH and seawater. At a current density of 10 mA cm^{-2}, the overpotentials for HER and OER were 149.7 mV and 198 mV, respectively. In an alkaline seawater electrolysis environment at a current density of 10 mA cm^{-2}, the overpotential for HER was 154.5 mV and that for OER was 182.5 mV. Wang [29] et al. successfully synthesized a heterostructured electrocatalyst Co-Ni_3Se_2/MoS_2/Ni_3S_2 constructed by Co-doped Ni_3Se_2, MoS_2, and Ni_3S_2 through a three-step hydrothermal method (hydroxide precursor preparation, selenization, and sulfidation). In a 1 mol/L KOH + seawater system, the OER achieved a current density of 10 mA cm^{-2} with an overpotential of only 164 mV, demonstrating excellent reaction kinetics [30]. Wang et al. prepared a novel ruthenium-doped bimetallic oxide (Ru-$NiCo_2O_4$) catalyst on conductive NF via a multi-step hydrothermal reaction, ion exchange, and subsequent annealing process. In alkaline media, the catalyst exhibits overpotentials of only 25 mV for HER and 249 mV for OER at a current density of 10 mA cm^{-2}. The constructed two-electrode alkaline electrolyzer requires merely 1.55 V to achieve a current density of 10 mA cm^{-2} [31]. Yao et al. synthesized a $NiFe_2O_4$/NiO/NF electrocatalyst with a rose-like crystalline/amorphous heterostructure on NF through a simple two-step thermal annealing method. In 1.0 M KOH electrolyte, the catalyst demonstrates excellent performance for OER, achieving overpotentials of only 122 mV and 145 mV at current densities of 20 mA cm^{-2} and 100 mA cm^{-2}, respectively, with stability exceeding 168 h.

NiFe-LDH is a two-dimensional layered material composed of nickel (Ni^{2+}) and iron (Fe^{3+}), featuring tunable metal ratios, a high specific surface area, and interlayer anion exchange capacity. Its unique structure endows it with excellent electrocatalytic performance, particularly high activity and stability in OER, making it a low-cost alternative catalyst to noble metals (IrO_2/RuO_2) for hydrogen production via water electrolysis. Li et al. [32] successfully prepared the NiFe-LDH electrocatalyst, which exhibits outstanding performance in the field of hydrogen production through water electrolysis. In a 1.0 M KOH electrolyte, the NiFe-LDH-4 catalyst demonstrates excellent OER performance, requiring only an overpotential of 235 mV at a current density of 50 mA cm^{-2} with a Tafel slope of 80.32 mV dec^{-1}; it also possesses a certain HER capability. In an alkaline seawater electrolyte, it not only maintains excellent OER performance but also shows a significant enhancement in HER performance. Compared with the 1.0 M KOH electrolyte, the HER overpotential at a current density of −10 mA cm^{-2} is reduced by 88.5 mV, and the Tafel slope is decreased by 53.6 mV dec^{-1}. Additionally, the catalyst exhibits good stability, enabling stable OER operation at a current density of 500 mA cm^{-2} in the 1.0 M KOH electrolyte, and an AEMWE (Anion Exchange Membrane Water Electrolyzer) device has also been constructed. This achievement provides an important reference for the development of low-cost, high-efficiency, and stable catalysts for hydrogen production via water electrolysis, and is of great significance for promoting the development of the hydrogen energy industry, especially the practical application of hydrogen production through seawater electrolysis [33]. Chen et al. fabricated a hierarchically structured CoO-Co_4N@NiFe-LDH heterojunction electrode on NF through a three-step hydrothermal-nitridation-electrodeposition approach. In 1 M KOH electrolyte, at a current density of 10 mA cm^{-2}, the overpotentials for HER and OER are 66 mV and 231 mV, respectively. When this electrode is employed as both the anode and cathode to assemble an alkaline electrolyzer, it only requires 1.529 V to achieve a current density of 10 mA cm^{-2} and maintains stable performance for 28 h [34]. Huang et al. constructed a Mo-CoN@NiFe-LDH Mott-Schottky heterojunction catalyst by coupling molybdenum-doped cobalt nitride (Mo-CoN) with NiFe-LDH, aiming to overcome the performance limitations of single-component catalysts in HER, OER, and UOR. In 1 M KOH, the overpotentials for HER and OER are only 76 mV and 257 mV, respectively, at a current density of 100 mA cm^{-2} [35]. Chang et al. constructed a self-supported p-n junction catalytic electrode NiCoP@NiFe LDH/NF on NF substrate via a two-step electrodeposition method. For OER, it exhibits an overpotential of 388 mV at a current density of 100 mA • cm^{-2}, and for HER, an overpotential of 132 mV at 10 mA • cm^{-2}. When used as both the anode and cathode in a two-electrode electrolyzer, it only requires 1.61 V to achieve a full water splitting current density of 10 mA • cm^{-2} [36]. Zang et al. designed an amorphous-crystalline heterostructured catalyst a-CoS@NiFe-LDH, which is composed of amorphous cobalt sulfide (a-CoS) and crystalline NiFe-LDH, for efficient OER. In a 1 M KOH electrolyte, it delivers an OER overpotential of only 221 ± 14 mV at a current density of 20 mA • cm^{-2} with a Tafel slope of 83.1 mV • dec^{-1}, along with excellent stability.

Most catalysts exhibit good performance and stability only in pure freshwater. However, natural freshwater accounts for a relatively low proportion of the Earth's water resources, while seawater makes up as high as 97 %, offering a potential option for large-scale industrial hydrogen production. Nevertheless, seawater electrolysis faces enormous challenges that require suitable electrocatalysts to reduce the activation energy of reactions. The main difficulty is that pollutants such as inorganic salt ions and microorganisms in seawater can block the active sites of catalytic materials, leading to catalyst deactivation [37]. During seawater electrolysis, OER requires high energy input to compete with the chlorine evolution reaction. Additionally, due to the low conductivity of seawater, there is significant energy loss during electrolysis, so the economic feasibility of direct seawater electrolysis for hydrogen production still needs to be considered. Therefore, there is an urgent need to establish standard seawater electrolyte systems and evaluation

indicators, as well as develop high-performance electrocatalysts [38]. In recent years, extensive discussions have been conducted on the feasibility of direct seawater electrolysis for hydrogen production [39]. To address challenges such as chloride ion corrosion and active site blockage in seawater electrolysis, Samikannu et al. prepared a bifunctional electrocatalyst Se-NiMnS_x@SC/NF with a hollow cycad cone structure via pyrolysis of LDPE waste, hydrothermal reaction, and selenization-sulfurization processes. In a 1.0 mol/L KOH + seawater system, the catalyst achieves overpotentials of 146 mV for HER and 262 mV for OER at a current density of 500 mA • cm^{-2}. The overall water splitting system constructed with it as both anode and cathode requires only 1.30 V and 2.07 V to reach current densities of 10 mA • cm^{-2} and 500 mA • cm^{-2}, respectively, and maintains a Faraday efficiency close to 100 % during 100 h of continuous operation [40]. Wu et al. prepared a NF-supported Fe-doped $CoMoO_4$ and Ni_3S_2 composite electrode (Fe-$CoMoO_4$/Ni_3S_2/NF) via a two-step hydrothermal method. In a 1 M KOH + seawater system, the electrode exhibits HER and OER overpotentials of 71 mV and 286 mV, respectively, at a current density of 10 mA • cm^{-2}, and retains its activity during a 15-h stability test [41]. By adjusting the Co-Fe ratio, Wu et al. synthesized a composite bifunctional electrocatalyst P-Fe_7S_8@Co_9S_8@Ni_3S_2/NF through a two-step hydrothermal doping-calcination method. In an alkaline seawater system, the catalyst shows HER and OER overpotentials of 89 mV and 288 mV, respectively, at a current density of 10 mA • cm^{-2}, along with long-term operational stability for 15 h.

There is a difference in electronegativity between selenium and Ni/Co. The introduction of selenium can adjust the electronic state of active sites, and such electron rearrangement can optimize the adsorption strength of the catalyst for M − OH and M − O in the OER process. After the combination of $Co_{0.5}Ni_{0.5}Se_2$ and NiCo-LDH, "conductive channels" are formed inside the material. Meanwhile, the bonding between selenium and Ni/Co may cause lattice distortion, generating more defect sites (i.e., highly active catalytic centers) and directly increasing the total number of active sites involved in the reaction. The Ni-Se and Co-Se bonds formed between selenium and Ni/Co have high bond energies, which can reinforce the framework structure of the material and inhibit the stacking or peeling of the layered structure. NiFe-LDH blocks the direct contact between large-volume chloride ions and the inner core; although it cannot completely prevent this contact, it can significantly slow down the diffusion rate of Cl^- to the core material. The heterointerfaces formed in the $Co_{0.5}Ni_{0.5}Se_2$@NiFe-LDH composite structure induce directional electron transfer and redistribution. The electronic properties of Co and Ni in $Co_{0.5}Ni_{0.5}Se_2$ complement the electronic demands of Ni and Fe in NiFe-LDH, regulating the adsorption strength of catalytic intermediates and effectively reducing the energy barriers of processes such as OER. Additionally, Fe, as a highly active center, further enhances the reaction kinetics together with Ni and Co. Furthermore, the layered structure of NiFe-LDH provides a high specific surface area and abundant ion transport channels. The uniform anchoring of $Co_{0.5}Ni_{0.5}Se_2$ not only inhibits the interlayer agglomeration and peeling of LDH but also significantly reduces the charge transfer resistance. The $Co_{0.5}Ni_{0.5}Se_2$@NiFe-LDH catalyst prepared in this work can inhibit the chlorine evolution side reaction during seawater splitting and reduce the corrosion of active sites by chloride ions. In addition, the structure of the $Co_{0.5}Ni_{0.5}Se_2$@NiFe-LDH catalyst can repel cations such as magnesium ions and calcium ions adsorbed on its surface, avoiding the blockage of active sites.

In this work, the materials were synthesized via a hydrothermal route(Figure S1). The process began with the preparation of a bimetallic nickel-cobalt precursor through hydrothermal treatment. This was followed by a second hydrothermal ion-exchange step using selenium powder and sodium hydroxide to grow $Co_{0.5}Ni_{0.5}Se_2$ directly on nickel foam. The final composite, $Co_{0.5}Ni_{0.5}Se_2$@NiFe-LDH, was obtained by integrating NiFe-LDH into the structure. During the water splitting process of $Co_{0.5}Ni_{0.5}Se_2$@NiFe-LDH, the synergistic effect between the $Co_{0.5}Ni_{0.5}Se_2$ core and NiFe-LDH shell plays a crucial role, primarily manifested in HER and OER processes. In the HER process, a layer of H_2O is adsorbed on the surface of $Co_{0.5}Ni_{0.5}Se_2$. At this stage, electron transfer through the active sites (Ni and Co) enables the dissociation of H_2O to generate H^+, which subsequently combines to form H_2 for desorption. The high electrical conductivity of $Co_{0.5}Ni_{0.5}Se_2$ reduces the energy barrier incurred during this process, thereby ensuring the efficient progression of the HER. As the core reaction zone for the OER, the NiFe-LDH shell undergoes sequential reactions: initially, a large number of OH^- are adsorbed on the catalyst surface and combine with metal sites (M = Ni, Fe) to form M − OH intermediates with the release of electrons. Subsequently, M − OH reacts with other OH^- to produce M − O intermediates and H_2O. Furthermore, surface reconstruction occurs at the heterogeneous interface formed between the $Co_{0.5}Ni_{0.5}Se_2$ core and NiFe-LDH shell, leading to the formation of M-OOH (M = Ni, Co, Fe) intermediates. Finally, M-OOH reacts with OH^- to generate O_2. Throughout this process, both NiFe-LDH and $Co_{0.5}Ni_{0.5}Se_2$ synergistically reduce the energy barrier of the OER, thereby accelerating the reaction kinetics. The resulting catalyst demonstrated promising electrocatalytic performance in an alkaline electrolyte. For HER, it exhibited an overpotential of 219 mV and a Tafel slope of 42.87 mV·dec^{-1} at a current density of 50 mA cm^{-2}. Meanwhile, OER occurred at an overpotential of 247 mV with a Tafel slope of 46.01 mV dec^{-1} under the same conditions. When evaluated in an alkaline seawater electrolyte, a slight degradation in performance was observed, attributable to the presence of chloride ions. At 50 mA cm^{-2}, the HER overpotential increased to 223 mV with a Tafel slope of 58.14 mV dec^{-1}, while the OER required an overpotential of 249 mV and showed a Tafel slope of 54.33 mV dec^{-1}.

2. Experimental

2.1. Preparation of NiCo-LDH materials

2.4 mmol of nickel nitrate, 1.2 mmol of cobalt nitrate, 4 mmol of ammonium fluoride, and 10 mmol of urea were weighed and dissolved in 40 mL of deionized water with stirring. Subsequently, the nickel foam was vertically immersed in the solution, which was then transferred to a stainless-steel autoclave and placed in an oven, maintaining a temperature of 120 °C for 6 h. After the reaction was completed and cooled, the sample was rinsed repeatedly more than 3 times and dried in an oven at 60 °C for 6 h.

2.2. Preparation of $Co_{0.5}Ni_{0.5}Se_2$ materials

2 g of sodium hydroxide and 0.3 g of selenium powder were dissolved in 50 mL of deionized water. After thorough stirring, the mixture was transferred to a stainless-steel autoclave and placed in a drying oven, maintaining a temperature of 200 °C for 8 h. Once the autoclave cooled to room temperature, the sample prepared in step 2.1 was immersed in the above solution, then transferred again to the drying oven for a hydrothermal reaction at 120 °C for 8 h. After the reaction was completed and cooled, the sample was rinsed repeatedly more than 3 times and dried in an oven at 60 °C for 6 h.

2.3. Preparation of $Co_{0.5}Ni_{0.5}Se_2$ @NiFe-LDH materials

1 mmol of iron nitrate, 4 mmol of nickel nitrate, 4 mmol of ammonium fluoride, and 10 mmol of urea were dissolved in 50 mL of deionized water and stirred until uniformly mixed. Subsequently, the prepared $Co_{0.5}Ni_{0.5}Se_2$ material was vertically immersed in the solution, which was then transferred to a stainless-steel autoclave and placed in a drying oven, maintaining a temperature of 120 °C for 8 h. After the reaction was completed and cooled, the sample was rinsed repeatedly more than 3 times and dried in an oven at 60 °C for 6 h.

2.4. Material characterization

The morphology and crystal structure of the as-prepared products were characterized by X-ray powder diffraction (XRD), scanning electron microscopy (SEM, Gemini 300-71-31), X-ray photoelectron spectroscopy (XPS), and transmission electron microscopy (TEM).

2.5. Material performance characterization

Electrocatalytic performance was evaluated using a CHI760F electrochemical workstation (Shanghai Chenhua) in alkaline electrolytes containing 1.0 M KOH and 1.0 M KOH with seawater. A series of electrochemical techniques—including cyclic voltammetry (CV), linear sweep voltammetry (LSV), electrochemical impedance spectroscopy (EIS), and cycling stability tests—were employed to characterize the catalytic behavior.

The synthesized material functioned as the working electrode, with a Hg/HgO electrode serving as the reference. Pt and graphite rods were used as counter electrodes for OER and HER, respectively. All recorded potentials were converted to the reversible hydrogen electrode (RHE) scale according to the following equation:

$$ERHE = EHg/HgO + 0.098 + 0.059 \times pH. \quad (2.1)$$

The corresponding overpotential (η) was calculated using:

$$\eta = ERHE - 1.23\ V. \quad (2.2)$$

3. Results and discussion

The crystal structure of the synthesized product was characterized by XRD. As shown in Fig. 1a, the diffraction peaks at 2θ = 44.4°, 51.6°, and 76.1° correspond to the nickel foam substrate (JCPDS No. 04–0850). The distinct diffraction peaks observed at 2θ = 19.04°, 33.03°, 38.45°, 38.65°, 51.95°, 58.99°, 59.52°, 62.59°, and 69.30° can be indexed to the (001), (100), (011), (002), (321), (012), (110), (003), and (111) planes of cobalt-nickel layered double hydroxide (JCPDS PDF#00-059-0461), respectively. Additionally, peaks located at 2θ = 11.41°, 22.97°, 33.53°, 33.42°, 38.99°, 45.98°, 59.94°, 61.25°, 65.13°, and 71.27° are consistent with the (003), (006), (101), (012), (015), (018), (110), (113), (116), and (119) planes of nickel-iron layered double hydroxide (JCPDS PDF#00-040-0215). Furthermore, the characteristic peaks detected at 2θ = 26.10°, 30.23°, 33.91°, 37.25°, 43.28°, 46.06°, 51.25°, 53.71°, 56.09°, and 58.40° match well with the (003), (006), (101), (012), (015), (018), (110), (113), (116), and (119) planes of $Co_{0.5}Ni_{0.5}Se_2$ (JCPDS PDF#04-001-6470). The collective presence of these diffraction features confirms the successful formation of the $Co_{0.5}Ni_{0.5}Se_2$@NiFe-LDH composite.

XPS was used to compare $Co_{0.5}Ni_{0.5}Se_2$, NiFe-LDH, and $Co_{0.5}Ni_{0.5}Se_2$@NiFe-LDH, aiming to investigate the elemental composition and interfacial electronic interactions within the structure of $Co_{0.5}Ni_{0.5}Se_2$@NiFe-LDH. The XPS survey spectrum (Figure S2) shows that $Co_{0.5}Ni_{0.5}Se_2$ contains Co, Ni, Se, and O elements, NiFe-LDH contains Ni, Fe, and O elements, and $Co_{0.5}Ni_{0.5}Se_2$@NiFe-LDH contains Co, Ni, Fe, Se, and O elements. The Co 2p X-ray photoelectron spectrum (Fig. 1b) can be decomposed into two pairs of doublets. The peaks at 797.67 eV and 790.79 eV are assigned to Co^{2+} $2p_{1/2}$ and Co^{3+} $2p_{1/2}$, respectively, while the peaks at 781.78 eV and 776.78 eV correspond to their $2p_{3/2}$ peaks, indicating the coexistence of Co^{2+} and Co^{3+}. Compared with $Co_{0.5}Ni_{0.5}Se_2$, the binding energy of the $2p_{3/2}$ orbital in $Co_{0.5}Ni_{0.5}Se_2$@NiFe-LDH increased by 0.89 eV, and the corresponding binding energy of the $2p_{1/2}$ orbital also increased, suggesting that electrons diffused from $Co_{0.5}Ni_{0.5}Se_2$ to $Co_{0.5}Ni_{0.5}Se_2$@NiFe-LDH [42]. The Ni 2p X-ray photoelectron spectrum (Fig. 1c) can be decomposed into two pairs of doublets. The peaks at 875.08 eV and 873.54 eV are attributed to Ni^{2+} $2p_{1/2}$ and Ni^{3+} $2p_{1/2}$, respectively, while the peaks at 857.35 eV and 855.93 eV correspond to their $2p_{3/2}$ peaks, indicating the coexistence of Ni^{2+} and Ni^{3+}. Compared with $Co_{0.5}Ni_{0.5}Se_2$, the binding energy of the $2p_{3/2}$ orbital in $Co_{0.5}Ni_{0.5}Se_2$@NiFe-LDH increased by 0.42 eV, and the corresponding binding energy of the $2p_{1/2}$ orbital also increased. Compared with NiFe-LDH, the binding energy of the $2p_{3/2}$ orbital in $Co_{0.5}Ni_{0.5}Se_2$@NiFe-LDH decreased by 2.27 eV, and the corresponding binding energy of the $2p_{1/2}$ orbital also decreased, indicating that $Co_{0.5}Ni_{0.5}Se_2$@NiFe-LDH accepted electrons from both $Co_{0.5}Ni_{0.5}Se_2$ and NiFe-LDH [43]. Fig. 1d shows the XPS spectrum of Fe 2p, with four peaks located at 706.93 eV, 712.42 eV, 718.55 eV, and 725.42

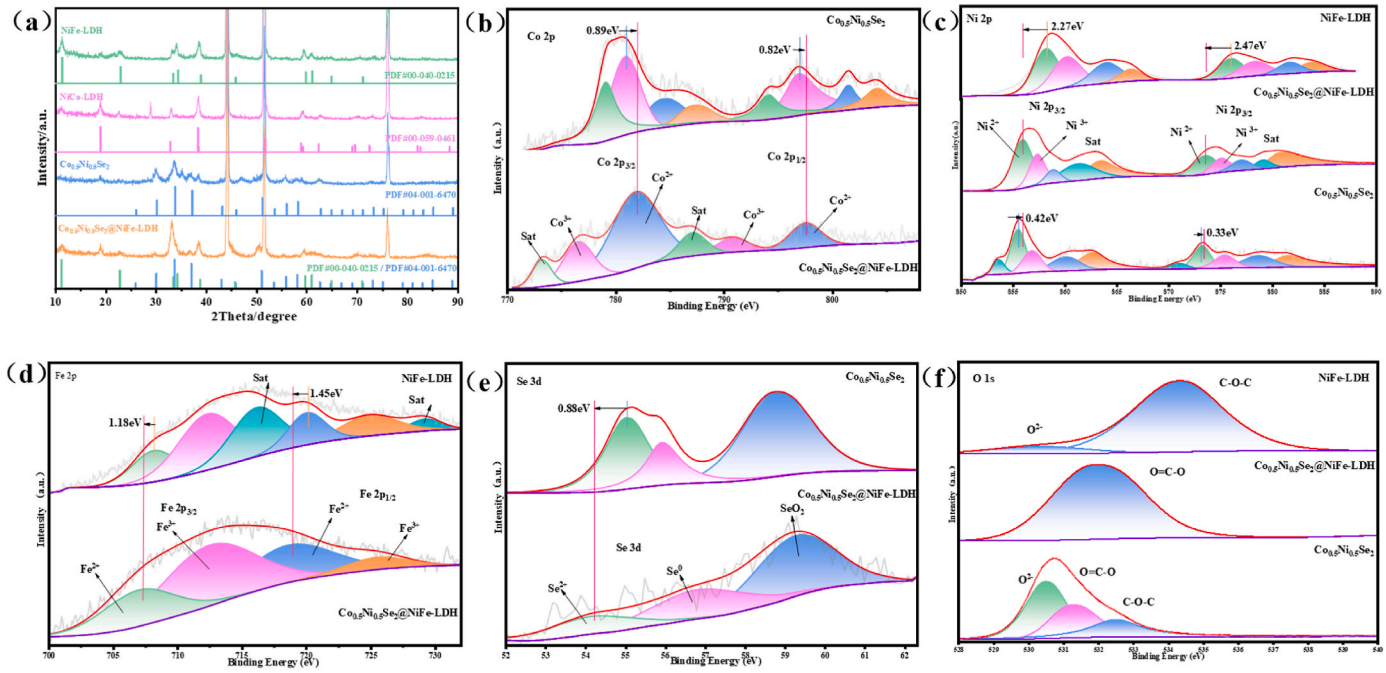

Fig. 1. (a) XRD patterns of the NiFe-LDH 、 NiCo-LDH 、 $Co_{0.5}Ni_{0.5}Se_2$ and $Co_{0.5}Ni_{0.5}Se_2$@NiFe-LDH (b) XPS of Co 2p in $Co_{0.5}Ni_{0.5}Se_2$ and $Co_{0.5}Ni_{0.5}Se_2$@NiFe-LDH (c) XPS of Ni 2p in NiFe-LDH 、 $Co_{0.5}Ni_{0.5}Se_2$ and $Co_{0.5}Ni_{0.5}Se_2$@NiFe-LDH (d) XPS of Fe 2p in NiFe-LDH and $Co_{0.5}Ni_{0.5}Se_2$ (e) XPS of Se 3d in $Co_{0.5}Ni_{0.5}Se_2$ and $Co_{0.5}Ni_{0.5}Se_2$@NiFe-LDH (f) XPS of C 1s in NiFe-LDH 、 $Co_{0.5}Ni_{0.5}Se_2$ and $Co_{0.5}Ni_{0.5}Se_2$@NiFe-LDH

eV, corresponding to the $2p_{3/2}$ and $2p_{1/2}$ spin-orbitals of Fe^{2+} and Fe^{3+}. Compared with NiFe-LDH, the binding energy of $Co_{0.5}Ni_{0.5}Se_2$@NiFe-LDH shifted negatively, indicating electron transfer through the interface and increased electron density [44–46]. As shown in Fig. 1e, the XPS spectrum of Se 3d shows that the peak at 54.13 eV in the Se 3d orbital corresponds to Se^{2-}, and 56.8 eV corresponds to Se^0. Compared with $Co_{0.5}Ni_{0.5}Se_2Co_{0.5}Ni_{0.5}Se_2$, the binding energy of $Co_{0.5}Ni_{0.5}Se_2$@NiFe-LDH shifted left, indicating electron transfer through the interface and increased electron density, while the broad peak at 59.24 eV is the oxidized state of surface Se [47,48]. Fig. 1f shows the comparison of O 1s XPS spectra, which is due to the oxidation reaction of the sample when exposed to air.

The microstructure and morphology of the samples were characterized using SEM. As shown in Fig. 2a, NiFe-LDH exhibits a flower-like aggregated architecture, demonstrating its macroscopic organizational features. Fig. 2b presents NiCo-LDH, which displays a well-defined nanostructure conducive to the observation of nanoscale morphological details. Fig. 2c illustrates $Co_{0.5}Ni_{0.5}Se_2$, where granular deposits are observed on the surface, indicating morphological evolution after the involvement of Se. Fig. 2d and e provide low- and high-magnification SEM images of the $Co_{0.5}Ni_{0.5}Se_2$@NiFe-LDH composite, respectively, highlighting its aggregated morphology and structural intricacies for improved understanding of the composite's micro-organization. Fig. 2f shows the energy-dispersive X-ray spectroscopy (EDS) elemental mapping of Co, Ni, Se, and Fe, where the distinct color-coded distributions clearly demonstrate uniform elemental composition and spatial dispersion, confirming the successful synthesis of a homogeneously integrated composite. Fig. 2(g–i) display TEM results of $Co_{0.5}Ni_{0.5}Se_2$@NiFe-LDH. Fig. 2g presents a low-magnification TEM overview of the material, with red and yellow boxes marking regions selected for high-resolution analysis. Fig. 2h shows the high-resolution transmission electron microscopy (HRTEM) image of $Co_{0.5}Ni_{0.5}Se_2$, with an interplanar spacing of 0.2643 nm, which corresponds to the (210) crystal plane index in the previous XRD pattern of $Co_{0.5}Ni_{0.5}Se_2$. Fig. 2i is the HRTEM image of NiFe-LDH, with an interplanar spacing of 0.2643 nm, corresponding to the (012) crystal plane index in the previous XRD pattern of NiFe-LDH.

HER performance of the synthesized catalysts was systematically evaluated in a 1.0 M KOH electrolyte. Fig. 3a displays the LSV curves of all catalysts recorded at a scan rate of 5 mV s^{-1}. $Co_{0.5}Ni_{0.5}Se_2$@NiFe-LDH hybrid demonstrated a low overpotential of 219 mV at 50 mA cm^{-2}, outperforming NiFe-LDH (268 mV), NiCo-LDH (227 mV), and $Co_{0.5}Ni_{0.5}Se_2$ (240 mV). Its performance is comparable to that of the Pt/C catalyst. Although the HER activity of $Co_{0.5}Ni_{0.5}Se_2$@NiFe-LDH is only slightly higher than that of $Co_{0.5}Ni_{0.5}Se_2$ and NiFe-LDH at a current density of 50 mA cm^{-2}, its overpotential is significantly better than the latter two at a current density of 100 mA cm^{-2} or even higher. From the data comparison in Figure S3, it is found that at a current density of 50 mA cm^{-2}, the HER performance data of the four groups of independent electrodes show little difference. This indicates that the $Co_{0.5}Ni_{0.5}Se_2$@NiFe-LDH catalyst has stable and reliable performance, and the excellent data is not accidental. A comparative bar chart of overpotentials at various current densities (Fig. 3b) further confirms the superior activity of $Co_{0.5}Ni_{0.5}Se_2$@NiFe-LDH, particularly at 10 and 100 mA cm^{-2}. Kinetic analysis based on the Tafel plots (Fig. 3c) revealed a Tafel slope of 42.87 mV dec^{-1} for $Co_{0.5}Ni_{0.5}Se_2$@NiFe-LDH, significantly lower than those of NiFe-LDH (97.56 mV dec^{-1}), NiCo-LDH

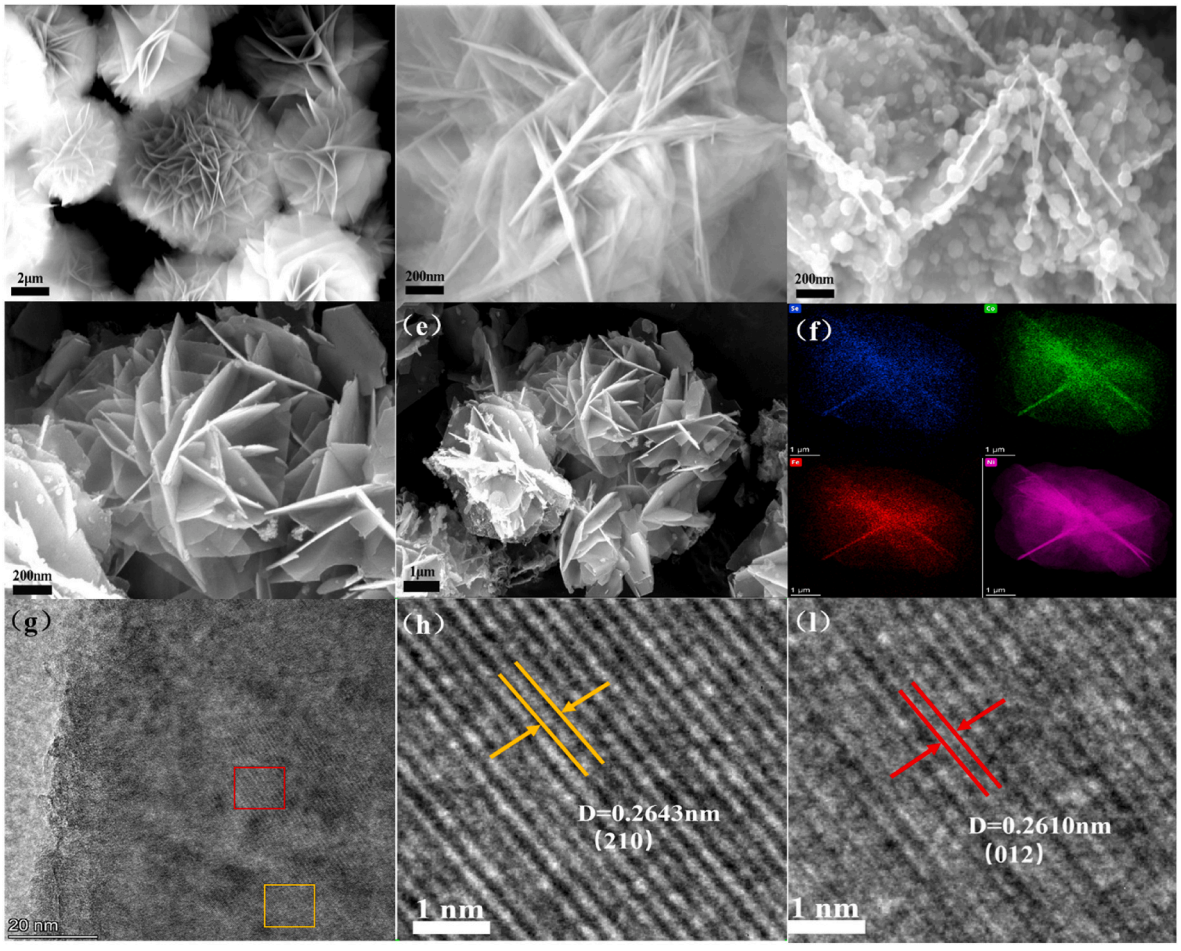

Fig. 2. Morphology and structure characterization of the as-prepared products (a) NiFe-LDH (b) NiCo-LDH (c) $Co_{0.5}Ni_{0.5}Se_2$ (d–e) $Co_{0.5}Ni_{0.5}Se_2$@ NiFe-LDH (f)EDS of $Co_{0.5}Ni_{0.5}Se_2$@ NiFe-LDH (g-i)TEM images of $Co_{0.5}Ni_{0.5}Se_2$@ NiFe-LDH.

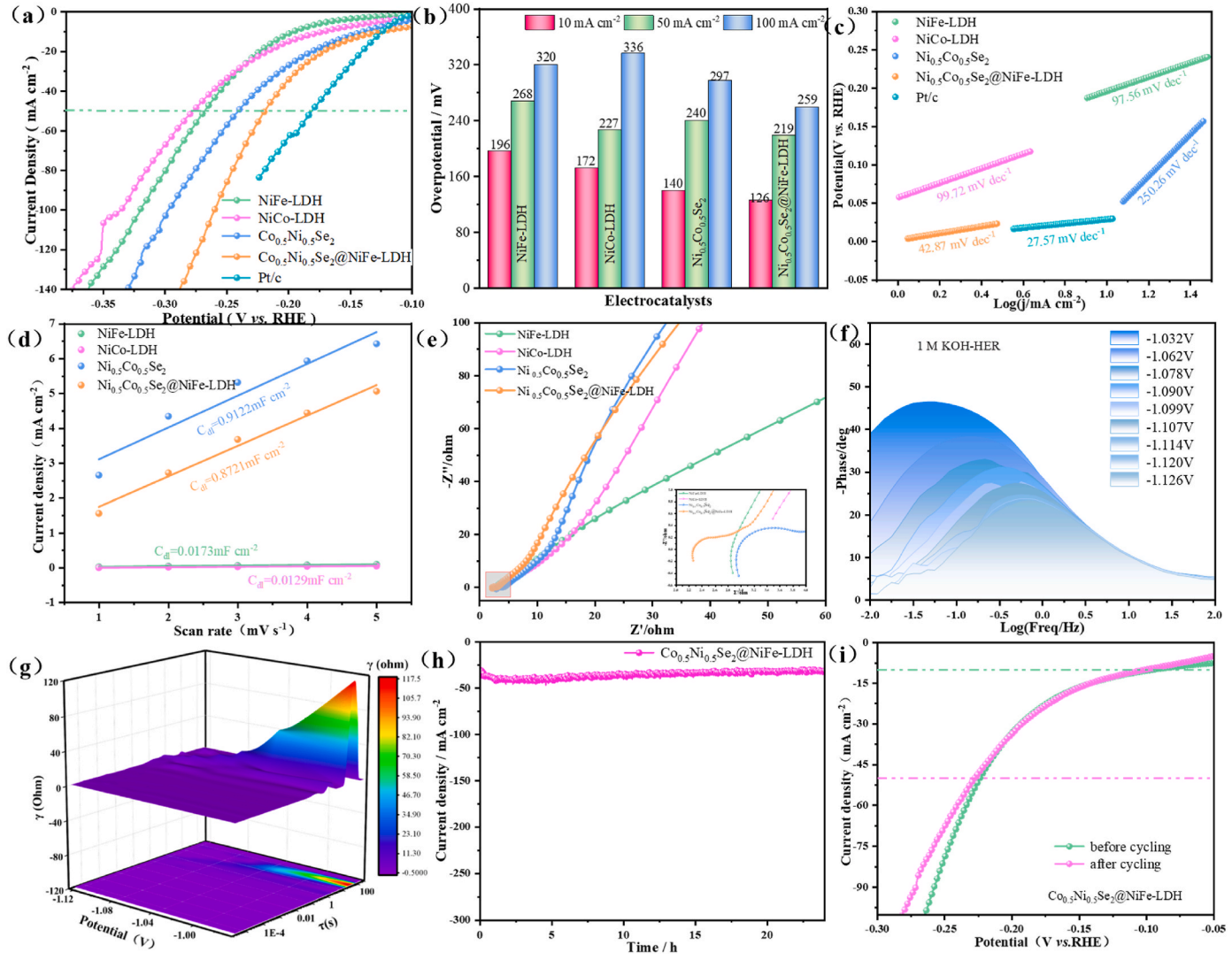

Fig. 3. HER performances (a) Polarization curves at scan rate (b)overpotential of electrode materials (c) Tafel plots (d) CV curves of double-layer capacitance (C_{dl}) (e) Nyquist plots HER performances (f) Bode plots at multiple voltages of HER(g)Distribution of Relaxation Times of HER(h-i)chronoamperometric stability tests, the insets is LSV curve after cyclingZ′ as a function of $\omega^{-1/2}$.

(99.72 mV dec^{-1}), and $Co_{0.5}Ni_{0.5}Se_2$ (250.26 mV dec^{-1}), The Tafel slope of Pt/C catalyst is 27.57 mV dec^{-1}, and the $Co_{0.5}Ni_{0.5}Se_2$@NiFe-LDH catalyst is comparable to it, indicating more favorable HER kinetics. Recent reports have indicated that [49,50], the mechanism of the HER in alkaline electrolytes mainly follows the following three fundamental steps:

Volmer step

$$H_2O + M + e^- \rightarrow M - H_{ads} + OH^- \quad (3.1)$$

Heyrovsky step

$$H_2O + M - H_{ads} + e^- \rightarrow H_2 + M + OH^- \quad (3.2)$$

Tafel step

$$2M - H_{ads} \rightarrow 2M + H^2 \quad (3.3)$$

Herein, M denotes a metal atom and H_{ads} represents a hydrogen atom adsorbed on the active site of the catalyst. Among the two aforementioned pathways, the Volmer step is indispensable. The reaction pathway of the catalyst is generally determined by the Tafel slope: when the Tafel slope is less than 45 mV dec^{-1}, the reaction follows the Volmer–Tafel pathway, which features high energy efficiency; when the Tafel slope is greater than 75 mV dec^{-1}, the reaction follows the Volmer–Heyrovsky pathway. Based on the above analysis of reaction pathways, the hydrogen evolution reaction of $Co_{0.5}Ni_{0.5}Se_2$@NiFe-LDH follows the Volmer-Tafel steps. A smaller Tafel slope indicates that the HER in alkaline electrolytes proceeds more readily. This advantage originates from the 3D structure constructed on NF. In addition, the large specific surface area and excellent electrical conductivity of $Co_{0.5}Ni_{0.5}Se_2$@NiFe-LDH also improve the efficiency of the entire catalytic process, including the Volmer reaction and the Heyrovsky/Tafel reaction. The electrochemical active surface area (ECSA), estimated from double-layer capacitance (C_{dl}), was used to evaluate active site exposure. As shown in Fig. 3d, $Co_{0.5}Ni_{0.5}Se_2$@NiFe-LDH exhibited a C_{dl} value of 0.8721 mF cm^{-2}, substantially higher than other catalysts, suggesting a greater number of accessible active sites. The nearly unchanged CV curve shapes across scan rates confirm electrochemical stability. EIS measurements performed between 100 kHz and 0.01 Hz (Fig. 3e) revealed a smaller semicircle diameter in the high-frequency region for $Co_{0.5}Ni_{0.5}Se_2$@NiFe-LDH, indicating reduced charge transfer resistance. In the low-frequency region, Z_w is attributed to the diffusion resistance of OH^- ions. modeled by Equation:

$$Z = Rs + Rct + \sigma w \omega^{-1/2} \quad (3.4)$$

where σ_w represents the Warburg coefficient, ω denotes the angular

frequency, and Z corresponds to the diffusion resistance of OH^- ions. The Bode plot in Fig. 3f shows a decreasing phase angle with increasing potential, implying accelerated electron transfer, especially at higher potentials. The distribution of relaxation times (DRT) analysis (Fig. 3g) revealed potential-dependent relaxation processes. At low potentials (−1.12 V), all processes contributed minimally to impedance, whereas a prominent peak emerged at higher potentials and longer relaxation times, indicating a kinetically significant step. Long-term stability tests (Fig. 3h–i) demonstrated excellent durability of $Co_{0.5}Ni_{0.5}Se_2$@NiFe-LDH, with only marginal increase in overpotential after 24 h of continuous operation, confirming its structural and catalytic robustness.

OER performance of the synthesized catalysts was systematically investigated in a 1.0 M KOH electrolyte. Fig. 4a presents the LSV curves of all catalysts measured at a scan rate of 2 mV s^{-1}. The $Co_{0.5}Ni_{0.5}Se_2$@NiFe-LDH hybrid demonstrated a low overpotential of 247 mV at 50 mA cm^{-2}, superior to those of NiFe-LDH (256 mV), NiCo-LDH (329 mV), and $Co_{0.5}Ni_{0.5}Se_2$ (313 mV). Furthermore, the overpotential of the $Co_{0.5}Ni_{0.5}Se_2$@NiFe-LDH catalyst is superior to that of the IrO_2 catalyst. Although the OER activity of $Co_{0.5}Ni_{0.5}Se_2$@NiFe-LDH is only slightly higher than that of $Co_{0.5}Ni_{0.5}Se_2$ and NiFe-LDH at 50 mA cm^{-2}, overall, the composite-structured $Co_{0.5}Ni_{0.5}Se_2$@NiFe-LDH exhibits higher activity than the single-component $Co_{0.5}Ni_{0.5}Se_2$ and NiFe-LDH. Combined with the previous TEM characterization results, NiFe-LDH is uniformly coated on the surface of $Co_{0.5}Ni_{0.5}Se_2$, forming a stable heterogeneous interface. $Co_{0.5}Ni_{0.5}Se_2$ improves electrical conductivity, while NiFe-LDH increases catalytic active sites, which reflects the structural-level synergy. From the data comparison in Figure S4, it is observed that at 50 mA cm^{-2}, the OER performance data of the four groups of independent electrodes exhibit slight variations. This demonstrates that the $Co_{0.5}Ni_{0.5}Se_2$@NiFe-LDH catalyst possesses stable and reliable performance, and the outstanding data is not coincidental. Comparative analysis of overpotentials at various current densities (Fig. 4b) further confirmed the outstanding activity of $Co_{0.5}Ni_{0.5}Se_2$@NiFe-LDH, particularly at 10 and 100 mA cm^{-2}. Tafel analysis (Fig. 4c) revealed a slope of 46.01 mV dec^{-1} for $Co_{0.5}Ni_{0.5}Se_2$@NiFe-LDH, lower than those of NiFe-LDH (51.38 mV dec^{-1}), NiCo-LDH (79.02 mV dec^{-1}), $Co_{0.5}Ni_{0.5}Se_2$ (103.09 mV dec^{-1}) and IrO_2 (95.03 mV dec^{-1}). Indicating more favorable OER kinetics. According to previously reported work [49,50], the mechanism of the OER mainly follows one of the two pathways described below, with the reaction equations presented as follows:

$$OH^- \rightarrow M - OH + e^- \tag{3.5}$$

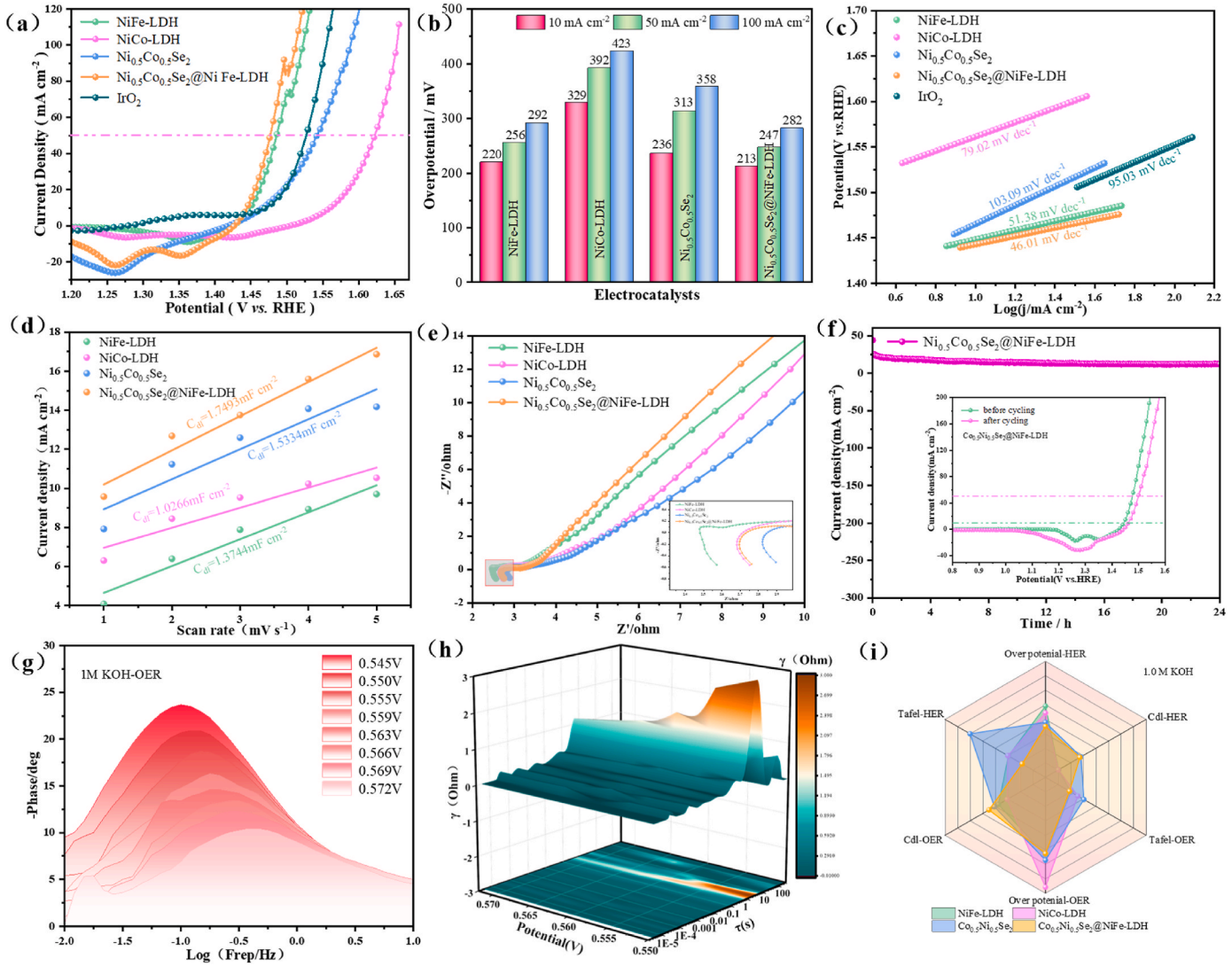

Fig. 4. OER performances (a) Polarization curves at scan rate (b)overpotential of electrode materials (c) Tafel plots (d) CV curves of double-layer capacitance (C_{dl}) (e) Nyquist plots OER performances (f)chronoamperometric stability tests, the insets is LSV curve after cyclingZ′ as a function of $\omega^{-1/2}$ (g) Bode plots at multiple voltages of OER(h)Distribution of Relaxation Times of OER(i)Radar chart in 1.0 M KOH.

$$M - OH + OH^- \rightarrow M - O + H_2O + e^- \quad (3.6)$$

$$2M - O \rightarrow 2M + O_2 \quad (3.7)$$

$$M - O + OH^- \rightarrow M - OOH + e^- \quad (3.8)$$

$$M - OOH \rightarrow M + O_2 + H^+ + e^- \quad (3.9)$$

M denotes the metal active site. Analogous to the aforementioned equation, the oxygen evolution reaction (OER) pathway over the $Co_{0.5}Ni_{0.5}Se_2$@NiFe-LDH catalyst proceeds as follows: OH^- is adsorbed onto the active sites to form M − OH intermediates, which is subsequently followed by the formation of M − O species on the catalyst surface that directly release O_2, or alternatively, the generation of M-OOH intermediates on the active surface that mediate the indirect release of O_2.The ECSA, evaluated through C_{dl}, revealed a C_{dl} value of 1.7493 mF cm^{-2} for $Co_{0.5}Ni_{0.5}Se_2$@NiFe-LDH (Fig. 4d), substantially exceeding those of other catalysts and suggesting greater exposure of active sites. The minimal variation in CV curve shapes across scan rates confirms electrochemical stability. EIS measurements conducted between 100 kHz and 0.01 Hz (Fig. 4e) showed a smaller semicircle diameter in the high-frequency region for $Co_{0.5}Ni_{0.5}Se_2$@NiFe-LDH, in the electrocatalytic water splitting system, the impedance response in the low-frequency region is mainly governed by ion diffusion in the electrolyte and the mass transfer process of gas evolution on the electrode surface, while the high-frequency region directly reflects the charge transfer at the electrolyte interface and the double-layer charging behavior. As shown in Figure S5, $Co_{0.5}Ni_{0.5}Se_2$@NiFe-LDH exhibits a smaller charge R_{ct} = 0.79 Ω and R_s = 1.421 Ω compared with $Co_{0.5}Ni_{0.5}Se_2$ (0.86 Ω, 1.573 Ω), NiCo-LDH (0.93 Ω, 1.671 Ω), and NiFe-LDH (0.92 Ω, 1.642 Ω). Meanwhile, C_{dl} of the above electrocatalysts was obtained from the corresponding semicircular plots, with values of 0.421 F cm^{-2} (NiCo-LDH), 0.483 F cm^{-2} ($Co_{0.5}Ni_{0.5}Se_2$), 0.485 F cm^{-2} (NiFe-LDH), and 0.592 F cm^{-2} ($Co_{0.5}Ni_{0.5}Se_2$@NiFe-LDH). The Warburg impedance was derived from the 45° linear segments, yielding 1.207 Ω (NiFe-LDH), 1.643 Ω (NiCo-LDH), 1.264 Ω ($Co_{0.5}Ni_{0.5}Se_2$), and 1.008 Ω ($Co_{0.5}Ni_{0.5}Se_2$@NiFe-LDH) (Table S1). These results indicate that the composite sample effectively reduces the resistance, increases the double-layer capacitance, and enhances the electron transfer efficiency. Long-term stability tests (Fig. 4f) demonstrated excellent durability of the hybrid catalyst, with only a slight increase in overpotential after 24 h of continuous operation (inset LSV comparison), affirming its structural and catalytic robustness. The Bode plot (Fig. 4g) exhibited a decreasing phase angle as the potential increased from 0.545 V to 0.572 V, reflecting enhanced electron transfer efficiency—particularly pronounced at 0.572 V, which promotes catalytic activity. The three-dimensional DRT analysis (Fig. 4h) showed potential- and relaxation time-dependent γ distributions, highlighting a characteristic relaxation process that significantly contributes to the interfacial impedance. Finally, a radar chart (Fig. 4i) comprehensively compares the HER and OER performance metrics of all catalysts in 1.0 M KOH, providing an intuitive visualization of the overall electrocatalytic performance.

A series of characterizations were performed on the samples after cycling. Fig. 5a shows the in-situ activated XPS survey spectra of the $Co_{0.5}Ni_{0.5}Se_2$@NiFe-LDH catalyst before and after cycling, confirming the presence of Se, Ni, and Co elements before and after cycling. Fig. 5 (b–f) show the comparison of XPS spectra of each element before and after cycling, further confirming the good structural stability of the prepared sample. Fig. 5b shows Co 2p; after cycling, the peaks at 782.33 eV and 797.75 eV are assigned to Co^{2+} $2p_{3/2}$ and Co^{3+} $2p_{1/2}$, respectively. Compared with $Co_{0.5}Ni_{0.5}Se_2$@NiFe-LDH before cycling, the binding energy of the Co $2p_{3/2}$ orbital increased by 0.55 eV, and the corresponding binding energy of the $2p_{1/2}$ orbital also increased. During the cycle stability process, Co^{3+} was unstable under high current, reduced to Co^{2+}, with part dissolved in the electrolyte and the other part attached to the material surface. The Ni 2p XPS spectrum after cycling also contains three types of peaks. The peaks at 855.97 eV and 857.40 eV are assigned to Ni^{2+} $2p_{3/2}$ and Ni^{3+} $2p_{3/2}$, respectively, while the peaks at 873.59 eV and 875.00 eV correspond to their $2p_{1/2}$ peaks, indicating the coexistence of Ni^{2+} and Ni^{3+}. Compared with $Co_{0.5}Ni_{0.5}Se_2$@NiFe-LDH before cycling, the binding energy of the Ni $2p_{3/2}$ orbital only increased by 0.04 eV, and the corresponding binding energy of the $2p_{1/2}$ orbital also increased, which is negligible. Fig. 5d shows the XPS

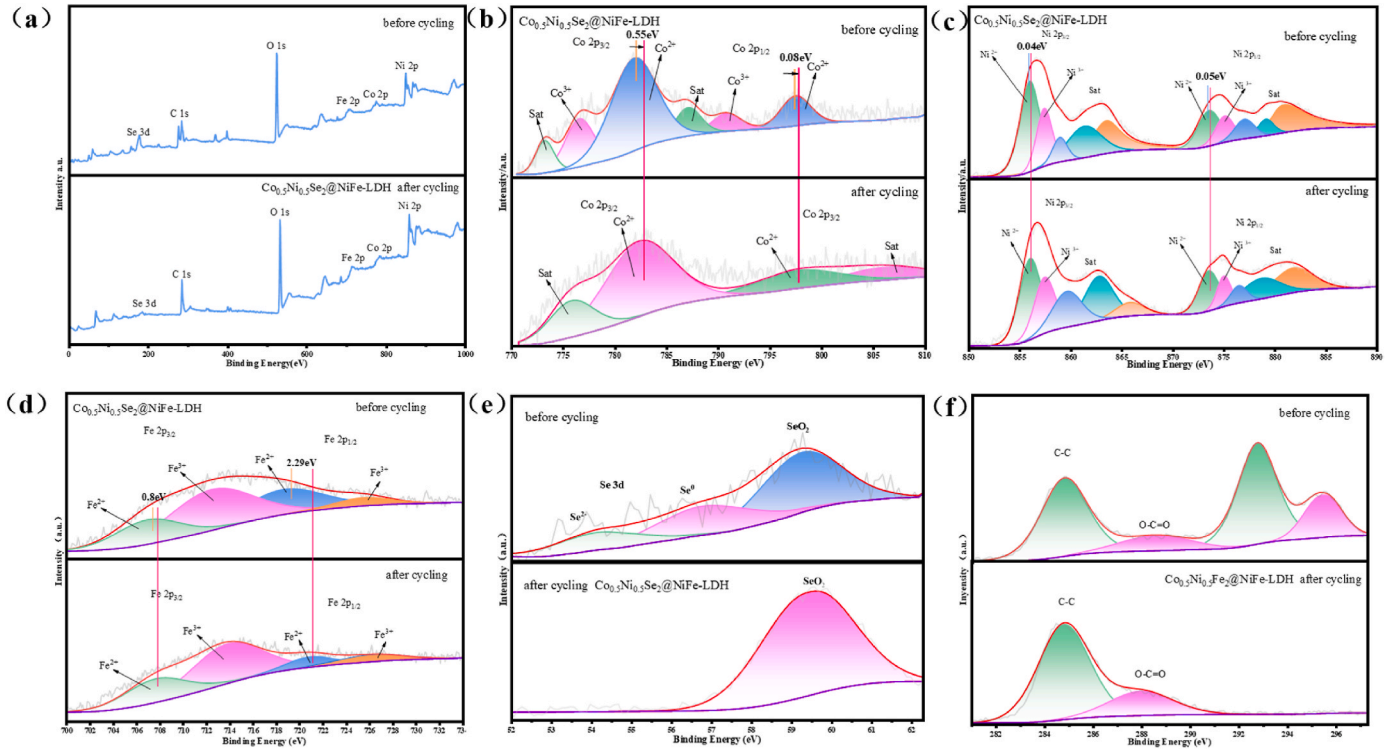

Fig. 5. XPS plot before and after cyclic stability test of $Co_{0.5}Ni_{0.5}Se_2$@ NiFe-LDH (a) XPS survey spectra (b)Co 2p (c) Ni 2p (d) Fe 2p (e) Se 3d (f) C 1s.

spectrum of Fe 2p, containing two types of peaks. Fe^{2+} and Fe^{3+} exist in Fe $2p_{3/2}$, with corresponding binding energies of 707.63 eV and 713.26 eV. In the Fe $2p_{1/2}$ channel corresponding to Fe $2p_{3/2}$, the binding energies of Fe^{2+} and Fe^{3+} are 720.84 eV and 726.14 eV, respectively. Compared with before cycling, the binding energy of the Fe $2p_{3/2}$ orbital in $Co_{0.5}Ni_{0.5}Se_2$@NiFe-LDH increased by 0.8 eV, and the corresponding binding energy of the $2p_{1/2}$ orbital also increased. As shown in Fig. 5e, the XPS spectrum of Se 3d shows that the broad peak at 59.39 eV is the oxidized state of surface Se. Fig. 5f shows the peak of C 1s.

To further confirm the excellent structural stability of the synthesized sample after cycling, SEM characterization was performed on the post-cycled material. As shown in the low-magnification SEM image (Fig. 6a) and the high-magnification image (Fig. 6d), the material largely retains its flower-like aggregated morphology without significant structural collapse after 24 h of cycling, indicating that the macroscopic structure of $Co_{0.5}Ni_{0.5}Se_2$@NiFe-LDH remains stable and is not substantially degraded by the electrochemical process. Some surface roughening can be observed, which is mainly attributed to the adsorption of a small amount of potassium hydroxide on the material surface after prolonged cycling, leading to enhanced charge transfer activity around the material during the electrochemical reactions. Fig. 6(b-c,e-f) show the elemental EDS mapping of the sample after cycling. The distributions of Se, Ni, Fe, and Co remain relatively uniform without obvious element aggregation, indicating that the compositional homogeneity and spatial distribution are well maintained after cycling, with no significant element migration or segregation. Based on these results, it can be concluded that the as-prepared product exhibits good structural stability. Fig. 6g–i presents TEM images of the cycled $Co_{0.5}Ni_{0.5}Se_2$@NiFe-LDH sample. Fig. 6g shows a low-magnification TEM image revealing the overall transmitted morphology. Fig. 6h shows the HRTEM image of $Co_{0.5}Ni_{0.5}Se_2$, with an interplanar spacing of 0.2643 nm. This value remains unchanged compared to that before cycling and corresponds to the (210) crystal plane index in the previous XRD pattern of $Co_{0.5}Ni_{0.5}Se_2$, indicating the stability of $Co_{0.5}Ni_{0.5}Se_2$@NiFe-LDH. Fig. 6i is the HRTEM image of NiFe-LDH, with an interplanar spacing of 0.2643 nm, which is slightly larger than that before cycling and corresponds to the (012) crystal plane index in the previous XRD pattern of NiFe-LDH. This is because the electrolyte causes slight corrosion of the sample and induces crystal defects during the long-cycle stability test, leading to an increase in lattice spacing.

The overall water splitting performance of all synthesized samples was systematically evaluated. Figure S6a presents the LSV curves of the optimal catalyst ($Co_{0.5}Ni_{0.5}Se_2$@NiFe-LDH) and the least active sample (NiCo-LDH), measured at a scan rate of 5 mV s^{-1}. Throughout the electrolysis process, vigorous generation of H_2 and O_2 bubbles was observed at the cathode and anode, respectively. The cycling stability was further assessed through chronoamperometric testing (Figure S6b). As depicted in Figure S6c, the voltage required to achieve 50 mA cm^{-2}

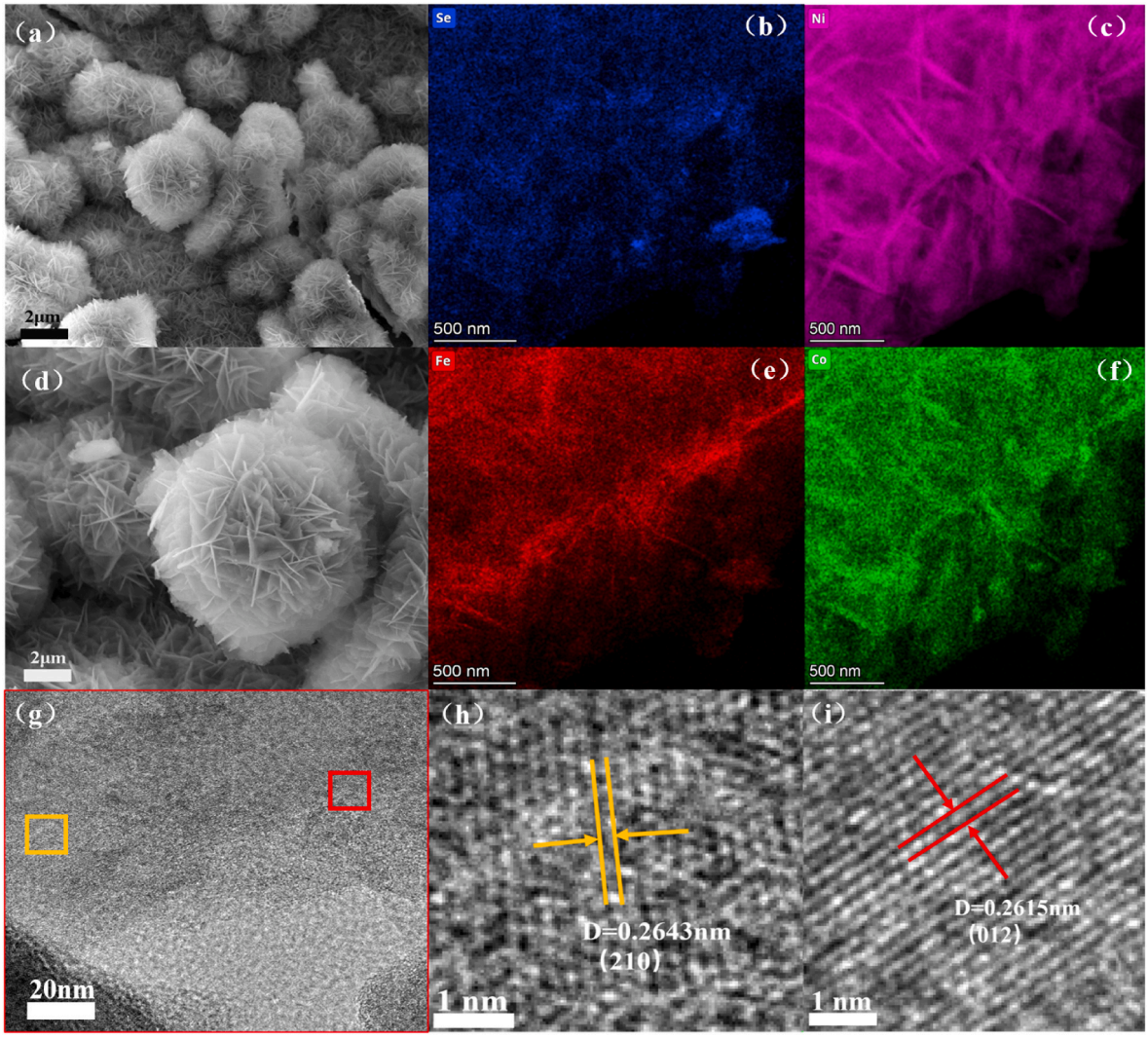

Fig. 6. Morphology and structure characterization of the as-prepared products (a,d) $Co_{0.5}Ni_{0.5}Se_2$@ NiFe-LDH(b,c,e,f)EDS of $Co_{0.5}Ni_{0.5}Se_2$@ NiFe-LDH (g-i)TEM images of $Co_{0.5}Ni_{0.5}Se_2$@ NiFe-LDH.

showed only a minimal increase from 1.73 V before cycling to 1.74 V after 30 h of continuous operation, demonstrating exceptional electrochemical durability. We also performed overall water splitting tests in seawater, selecting the $Co_{0.5}Ni_{0.5}Se_2$@NiFe-LDH catalyst with the lowest linear sweep voltammetry (LSV) value (Figure. S6d) for the measurements. It can be observed that the voltage is around 1.88 V at 50 mA cm^{-2} (Figure. S6e), which is slightly higher than that for overall water splitting in alkaline media (approximately 1.73 V). Additionally, we tested the overpotentials before and after the overall water splitting process (Figure. S6f), and the difference between the two overpotentials is only 0.0075 V, which is negligible. This indicates that the $Co_{0.5}Ni_{0.5}Se_2$@NiFe-LDH catalyst also exhibits excellent stability in seawater.

In conclusion, the $Co_{0.5}Ni_{0.5}Se_2$@NiFe-LDH electrocatalyst, synthesized via a hydrothermal route, exhibited excellent catalytic activity for both the HER and OER. The negligible change in overpotential after 24 h of cycling further confirms its remarkable stability. The $Co_{0.5}Ni_{0.5}Se_2$@NiFe-LDH catalyst effectively mitigates the following major issues during water splitting in seawater: For Mg^{2+}/Ca^{2+} fouling, the negatively charged NiFe-LDH layers generate electrostatic repulsion to reduce the initial adsorption of cations. $Co_{0.5}Ni_{0.5}Se_2$ increases surface roughness and promotes Fe redeposition to form dynamic local units that disrupt nucleation environments, with bubble scouring further inhibiting scaling; Regarding carbonate precipitation, NiFe-LDH selectively adsorbs and intercalates CO_3^{2-} to lower free concentrations. $Co_{0.5}Ni_{0.5}Se_2$ optimizes reaction kinetics to suppress CO_2 conversion to CO_3^{2-}, and the pores and large specific surface area of the heterostructure disperse and carry away a small amount of microcrystals; Against salinity-induced passivation, $Co_{0.5}Ni_{0.5}Se_2$ constructs efficient electron transport channels to enhance electron conduction efficiency, the strong interfacial interaction, synergistic electronic effects, and lattice distortion mitigation between the two components maintain structural integrity, reduce active site loss, and prevent passivation. Subsequent performance evaluations were conducted in an alkaline seawater electrolyte (1.0 M KOH + seawater, pH = 13.5), demonstrating its potential for practical applications in seawater splitting.

HER performance of the synthesized catalysts was systematically evaluated in an alkaline seawater electrolyte. Fig. 7a presents the LSV curves of all catalysts measured at a scan rate of 5 mV s^{-1}. The $Co_{0.5}Ni_{0.5}Se_2$@NiFe-LDH hybrid demonstrated a significantly lower overpotential of 223 mV at 50 mA cm^{-2} compared to NiFe-LDH (313 mV), NiCo-LDH (320 mV), and $Co_{0.5}Ni_{0.5}Se_2$(249 mV). The superior activity was further confirmed by the overpotential comparison shown in the bar chart (Fig. 7b). Kinetic analysis based on the Tafel plots (Fig. 7c) revealed a slope of 58.14 mV dec^{-1} for $Co_{0.5}Ni_{0.5}Se_2$@NiFe-LDH, which is substantially lower than those of NiFe-LDH (115.29 mV dec^{-1}), NiCo-LDH (137.73 mV dec^{-1}), and $Co_{0.5}Ni_{0.5}Se_2$ (109.21 mV

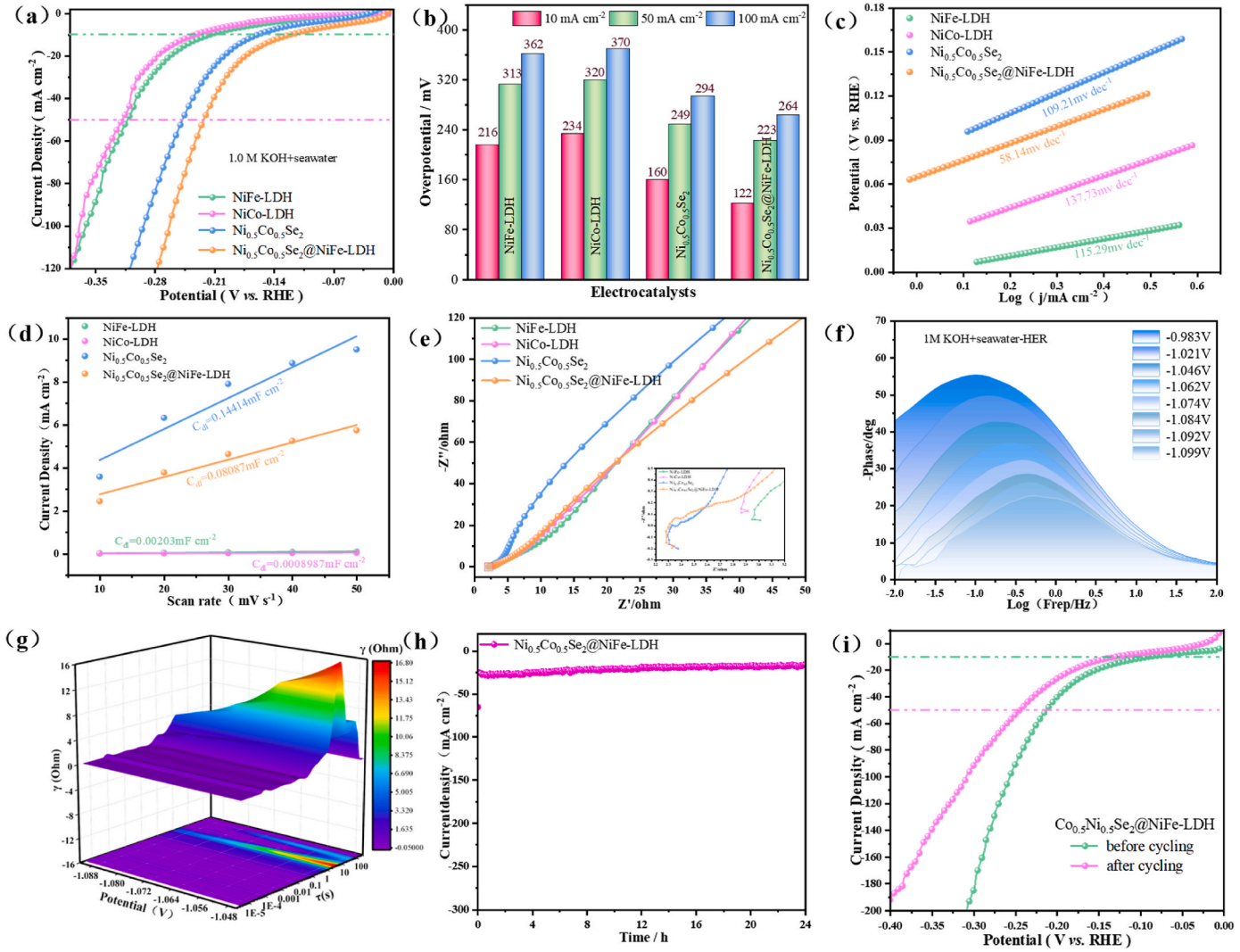

Fig. 7. HER performance in 1.0 M KOH and seawater (a) Polarization curves at scan rate (b)overpotential of electrode materials (c) Tafel plots (d) CV curves of double-layer capacitance (C_{dl}) (e) Nyquist plots HER performances (f) Bode plots at multiple voltages of HER(g)Distribution of Relaxation Times of HER(h-i) chronoamperometric stability tests, the insets is LSV curve after cyclingZ′ as a function of $\omega^{-1/2}$.

dec^{-1}), indicating more favorable HER kinetics. The ECSA, evaluated through C_{dl}. Fig. 7d shows the electric double-layer capacitance (EDLC) plots of the four groups of samples. It can be seen that the Cdl value of $Co_{0.5}Ni_{0.5}Se_2$@NiFe-LDH is 0.08087 mF cm^{-2}, which is higher than that of NiFe-LDH (0.00230 mF cm^{-2}) and NiCo-LDH (0.00089 mF cm^{-2}) but lower than that of $Co_{0.5}Ni_{0.5}Se_2$ (0.14414 mF cm^{-2}). This may be attributed to the high intrinsic activity of the catalyst. However, it still indicates that $Co_{0.5}Ni_{0.5}Se_2$@NiFe-LDH exposes a relatively large number of active sites. EIS results (Fig. 7e) demonstrated a steeper low-frequency slope for $Co_{0.5}Ni_{0.5}Se_2$@NiFe-LDH, indicating reduced ion diffusion resistance and improved charge transfer efficiency. The Bode plot (Fig. 7f) exhibited a decreasing phase angle with increasing potential, reflecting enhanced electron transfer efficiency—particularly pronounced at higher potentials, which promotes catalytic activity. The three-dimensional DRT analysis (Fig. 7g) showed potential- and time-dependent γ distributions, with a prominent high-γ region (red zone) observed at positive potentials and longer relaxation times, indicating a significant relaxation process contributing to the interfacial impedance. Long-term stability tests (Fig. 7h–i) confirmed the excellent durability of $Co_{0.5}Ni_{0.5}Se_2$@NiFe-LDH, with only minimal increase in overpotential after 24 h of continuous operation.

OER performance of the synthesized electrocatalysts was comprehensively evaluated in an alkaline seawater electrolyte. As shown in Fig. 8a, the LSV curves measured at a scan rate of 2 mV s^{-1} demonstrate that $Co_{0.5}Ni_{0.5}Se_2$@NiFe-LDH exhibits a notably lower overpotential of 249 mV at 50 mA cm^{-2} compared to NiFe-LDH (260 mV), NiCo-LDH (379 mV), and $Co_{0.5}Ni_{0.5}Se_2$ (314 mV). A comparative analysis of overpotentials further highlights the superior activity of the $Co_{0.5}Ni_{0.5}Se_2$@NiFe-LDH hybrid (Fig. 8b). A comparison of the LSV curves (Figure S7) shows that the overpotential in natural Bohai seawater is significantly higher than that in simulated seawater at the same current density. This indicates that factors such as ionic interference and impurity adsorption present in the natural seawater system exert a negative impact on electrocatalytic performance: they increase the reaction energy barrier, reduce the catalytic kinetic rate, and thus result in superior catalytic performance in simulated seawater. Tafel analysis (Fig. 8c) indicates favorable OER kinetics for $Co_{0.5}Ni_{0.5}Se_2$@NiFe-LDH, with a slope of 54.33 mV dec^{-1}, outperforming NiFe-LDH (73.82 mV dec^{-1}) and NiCo-LDH (88.69 mV dec^{-1}). The enhanced kinetics suggest efficient catalytic behavior during the oxygen evolution process. Fig. 8d presents the EDLC plots of the four groups of samples. It is observed that the Cdl value of $Co_{0.5}Ni_{0.5}Se_2$@NiFe-LDH is 0.06883 mF cm^{-2}, which is higher than that of $Co_{0.5}Ni_{0.5}Se_2$ (0.04232 mF cm^{-2}) and NiCo-LDH (0.06097 mF·cm$^{-2\text{-}2}$) but slightly lower than that of NiFe-LDH (0.07008 mF cm^{-2}). Nevertheless, it also demonstrates that $Co_{0.5}Ni_{0.5}Se_2$@NiFe-LDH exposes abundant active sites, which can enhance the

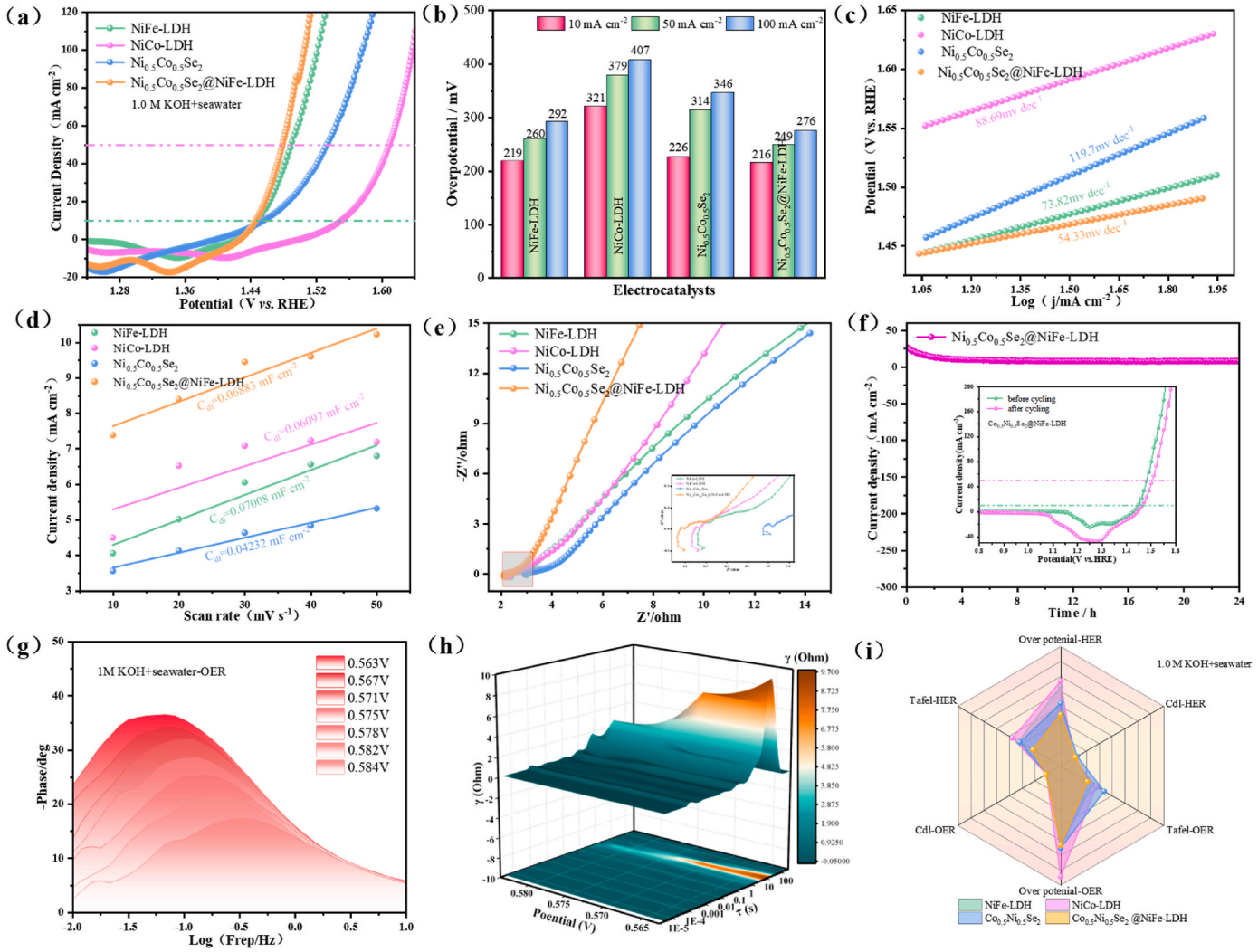

Fig. 8. OER performances in 1.0 M KOH and seawater (a) Polarization curves at scan rate (b)overpotential of electrode materials (c) Tafel plots (d) CV curves of double-layer capacitance (C_{dl}) (e) Nyquist plots OER performances (f)chronoamperometric stability tests, the insets is LSV curve after cyclingZ′ as a function of $\omega^{-1/2}$ (g) Bode plots at multiple voltages of OER(h)Distribution of Relaxation Times of OER(i)Radar chart in 1.0 M KOH.

catalytic performance. EIS performed from 100 kHz to 0.01 Hz (Fig. 8e) shows a smaller semicircle diameter in the high-frequency region for $Co_{0.5}Ni_{0.5}Se_2$@NiFe-LDH, indicating reduced charge transfer resistance and improved electron conduction. Long-term stability tests for both HER and OER (Fig. 8f) confirm the outstanding durability of $Co_{0.5}Ni_{0.5}Se_2$@NiFe-LDH, with only minimal activity loss after 24 h of continuous operation, as illustrated by the nearly overlapping LSV curves before and after cycling. The Bode phase plot (Fig. 8g) exhibits a decreasing phase angle with increasing potential (0.563 V–0.584 V), signifying accelerated electron transfer, particularly at 0.584 V, which is conducive to enhanced OER activity. DRT analysis (Fig. 8h) identifies potential- and time-dependent characteristics, with pronounced γ variations indicating a dominant relaxation process contributing significantly to the interfacial impedance under specific conditions. A radar chart summarizing the overall HER and OER performance of all samples in alkaline seawater electrolyte (1.0 M KOH + seawater) is presented in Fig. 8i, offering an intuitive comparison of the electrocatalytic capabilities across the synthesized materials. We further conducted a long-term stability test of seawater splitting at a high current density of 500 mA cm^{-2} (Figure S8). It can be seen that the voltage of $Co_{0.5}Ni_{0.5}Se_2$@NiFe-LDH stabilizes around 1.66 V at 500 mA cm^{-2}, which is almost identical to the overpotential (1.64 V) at the same current density in Figure S9. This confirms that the $Co_{0.5}Ni_{0.5}Se_2$@NiFe-LDH catalyst exhibits high performance and excellent stability in seawater under high current density. To fully evaluate the stability of the catalyst in seawater, we further performed a long-term cycling stability test at 500 mA cm^{-2} for 200 h (Figure S10). It can be observed that the $Co_{0.5}Ni_{0.5}Se_2$@NiFe-LDH catalyst maintains stable operation even under the conditions of high current density and extended duration. Table S2 compares the electrocatalytic performance of the prepared samples with previously reported catalysts, showing that $Co_{0.5}Ni_{0.5}Se_2$@NiFe-LDH exhibits lower overpotentials than other currently reported catalysts.

To investigate chlorine residues on the catalyst surface after cycling, we performed XPS measurements on $Co_{0.5}Ni_{0.5}Se_2$@NiFe-LDH. Table S3 lists the atomic percentages of each element, and Figure S11 shows the survey spectrum. The results indicate that the chlorine content is 0.18 %. In the survey spectrum, besides the signals of characteristic elements (Co, Ni, Fe, Se, O, and C), a weak chlorine signal can be detected at a binding energy of approximately 200 eV, but the peak intensity is barely distinguishable. This suggests that while chlorine residues exist on the catalyst surface after reaction cycles, their content is extremely low and has a negligible impact on electrochemical performance. It should be noted that we cannot guarantee the complete absence of chlorine residues on the catalyst surface post-cycling—a major challenge that still persists for water splitting in seawater systems. Thus, the core objective of this work is to minimize chlorine residues on the catalyst surface to the greatest extent possible. Figures S12 (a-f) show the XPS spectra of each element. Compared with the XPS spectra in 1 M KOH, the binding energies of Ni 2p and Co 2p are collectively slightly shifted to the right, while those of Se 3d and Fe 2p are slightly shifted to the left. To verify the structural stability of $Co_{0.5}Ni_{0.5}Se_2$@NiFe-LDH during OER tests in an alkaline seawater system, TEM characterizations were performed on the catalyst after OER cycling. EDS mappings (Figs. S13a-d) reveal the uniform distribution of all elements on the catalyst surface, indicating the stable morphology and structure of the catalyst. Figs. S13e-g present the high-resolution TEM (HRTEM) images: Fig. S13f shows the HRTEM image of $Co_{0.5}Ni_{0.5}Se_2$ with an interplanar spacing of 0.2645 nm, which is consistent with that before cycling and corresponds to the (210) crystal plane index of $Co_{0.5}Ni_{0.5}Se_2$ in the previous XRD pattern. Fig. S13g displays the HRTEM image of NiFe-LDH, with an interplanar spacing of 0.2643 nm matching the (012) crystal plane index of NiFe-LDH in the prior XRD pattern. Compared with the lattice spacing before cycling, both values show an increase. This phenomenon is attributed to the adsorption of a small amount of ions from the electrolyte onto the catalyst surface during OER tests in seawater, which induces crystal defects inside the sample and consequently leads to the expansion of lattice spacing. An oxidation peak appears at the low potential region of the OER polarization curve for $Co_{0.5}Ni_{0.5}Se_2$@NiFe-LDH, indicating the occurrence of the CER. XPS and TEM characterizations were performed on the $Co_{0.5}Ni_{0.5}Se_2$@NiFe-LDH catalyst: in the XPS survey spectrum, besides the characteristic signals of elements such as Co, Ni, Fe, Se, O, and C, a weak signal of chlorine was detected at a binding energy of approximately 200 eV, yet the peak intensity was almost indistinguishable. This suggests that although chlorine residues exist on the catalyst surface after the reaction cycle, their content is extremely low, and the impact on electrochemical performance is negligible. Consistent with previous reports [40], although the HRTEM lattice fringes changed before and after the reaction, no blurring of the lattice fringes or agglomeration of nanoparticles was observed. These phenomena collectively demonstrate that the chlorine evolution reaction, which competes with the OER during seawater electrolysis, is effectively suppressed. Figure S14 displays the Raman spectrum of $Co_{0.5}Ni_{0.5}Se_2$@NiFe-LDH after OER cycling tests in 1 M KOH + seawater electrolyte. The Ni-OOH, Co-OOH, and Fe-OOH labeled in the pink area of the figure are active species in the OER reaction. Specifically, the peak around 454 cm^{-1} is assigned to the bending vibration of M − O (M = Ni/Co/Fe), the peak near 533 cm^{-1} corresponds to the stretching vibration of Ni-OOH/Co-OOH, and the peak around 719 cm^{-1} is attributed to the stretching vibration of the O-O bond in M-OOH. Based on these characteristic peaks, it can be concluded that $Co_{0.5}Ni_{0.5}Se_2$@NiFe-LDH forms active sites with a highly active hydroxyl oxide structure during OER performance testing in seawater.

After compositing $Co_{0.5}Ni_{0.5}Se_2$ with NiFe-LDH, the strong electronegativity difference between O and Se atoms alters the direction of electron transfer, which upshifts the d-band center of catalytically active sites. This enhances the kinetics of OH^- adsorption and O-O bond formation in the OER, while tuning the adsorption free energy of H^+ in the HER to a value close to the ideal. A highly efficient electron transport channel is constructed, which reduces the R_s and charge R_{ct} and improves the charge transfer efficiency. Furthermore, during water splitting in seawater, the formed Se-O coordinated heterointerfacial structure, via strong covalent bonding interactions, not only prevents Cl^- from undergoing ion exchange with interlayer ions but also inhibits the excessive generation of Ni^{3+}, thereby suppressing the CER.

4. Conclusion

In summary, a hierarchical $Co_{0.5}Ni_{0.5}Se_2$@NiFe-LDH composite with nanoflake-assembled flower-like architecture was successfully synthesized through a facile hydrothermal route. This rationally designed structure substantially enhances the electrochemical active surface area and provides abundant accessible active sites, leading to significantly improved electrocatalytic performance. The catalyst demonstrates exceptional activity for both the hydrogen evolution reaction (HER) and oxygen evolution reaction (OER) in 1 M KOH and alkaline seawater electrolytes, achieving a current density of 50 mA cm^{-2} at low overpotentials. Furthermore, it exhibits outstanding efficiency in overall water splitting applications. Notably, the catalyst maintains excellent structural and catalytic stability even after 24 h of continuous operation, with no evident morphological degradation. Compared with previous studies, this work can effectively inhibit the chlorine evolution reaction (CER) occurring during seawater splitting and block the clogging of active sites by other ions in seawater, thereby improving the performance of the catalytic material at high current densities. As a non-precious metal-based electrocatalyst, $Co_{0.5}Ni_{0.5}Se_2$@NiFe-LDH possesses notable advantages including cost-effectiveness, simple synthesis, high catalytic efficiency, and superior durability, highlighting its great potential for practical applications in sustainable energy conversion systems.

CRediT authorship contribution statement

Shuang-shuang Zhang: Writing – review & editing, Writing – original draft. **Yong-qi Tian:** Writing – review & editing. **Bo-yao Zhang:** Writing – review & editing. **Yu-wen Pan:** Writing – review & editing. **Yi-bo Wang:** Writing – review & editing. **Jun Xiang:** Writing – review & editing. **De-peng Zhao:** Writing – review & editing. **Rong-da Zhao:** Writing – review & editing. **Fu-fa Wu:** Writing – review & editing. **Li-hua Miao:** Writing – review & editing.

Declaration of competing interest

The authors declare that they have no known competing financial interests or personal relationships that could have appeared to influence the work reported in this paper.

Acknowledgment

This work was supported by the Project of Education Department of Liaoning Province (No. LJKMZ20220959), the National Natural Science Foundation of China(No. 51971106). Science and Technology Innovation Talent Project of Liaoning Provincial Department of Education (LJ222411632049).

Appendix A. Supplementary data

Supplementary data to this article can be found online at https://doi.org/10.1016/j.jpowsour.2025.239229.

Data availability

Data will be made available on request.

References

[1] R.Y. Li, S.L. Xu, Z.Q. Ai, J.G. Qi, F.F. Wu, R.D. Zhao, D.P. Zhao, Interface engineering accelerated surface reconstruction for electrocatalytic water splitting and energy storage device through hybrid structured $ZnCo_2O_4$@NiCo-LDH nanocomposite, Int. J. Hydrogen Energy 91 (2024) 867–876, https://doi.org/10.1016/j.ijhydene.2024.10.104.

[2] J.O.M. Bockris, T.N. Veziroglu, Estimates of the price of hydrogen as a medium for wind and solar sources, Int. J. Hydrogen Energy 32 (2007) 1605–1610, https://doi.org/10.1016/j.ijhydene.2007.04.037.

[3] X.M. Li, X.G. Hao, A. Abudula, G. Guan, Nanostructured catalysts for electrochemical water splitting: current state and prospects, J. Mater. Chem. A 4 (2016) 11973–12000, https://doi.org/10.1039/C6TA02334G.

[4] J. Greeley, T.F. Jaramillo, J. Bonde, I. Chorkendorff, J.K. Nørskov, Computational high-throughput screening of electrocatalytic materials for hydrogen evolution, Nat. Mater. 5 (2006) 909–913, https://doi.org/10.1038/nmat1752.

[5] Yu W. Pan, F.C. Zhao, G.N. Ji, S.L. Xu, R.Y. Li, H.Y. Zhou, R.D. Zhao, D.P. Zhao, F. F. Wu, Electrocatalytic performance of Ni-based high-entropy alloys with unique structural features in alkaline and seawater electrolysis under -10 °C, Int. J. Hydrogen Energy 127 (2025) 147–159, https://doi.org/10.1016/j.ijhydene.2025.04.071.

[6] Z.W. Seh, J. Kibsgaard, C.F. Dickens, I. Chorkendorff, J.K. Nørskov, T.F. Jaramillo, Combining theory and experiment in electrocatalysis: insights into materials design, Science 355 (2017) 4998, https://doi.org/10.1126/science.aad4998.

[7] T.F. Jaramillo, K.P. Jørgensen, J. Bonde, J.H. Nielsen, S. Horch, I. Chorkendorff, Identification of active edge sites for electrochemical H_2 evolution from MoS_2 nanocatalysts, Science 317 (2007) 100–102, https://doi.org/10.1126/science.1141483.

[8] L.C. Seitz, C.F. Dickens, K. Nishio, Y. Hikita, J. Montoya, A. Doyle, C. Kirk, A. Vojvodic, H.Y. Hwang, J.K. Norskov, T.F. Jaramillo, A highly active and stable $IrO_x/SrIrO_3$ catalyst for the oxygen evolution reaction, Science 353 (2016) 1011–1014, https://doi.org/10.1126/science.aaf5050.

[9] C.M. Wang, Q.H. Geng, L.L. Fan, J.X. Li, L. Ma, C.L. Li, Phase engineering oriented defect-rich amorphous/crystalline RuO_2 nanoporous particles for boosting oxygen evolution reaction in acid media, Nano Res. Energy 2 (2023) e9120070, https://doi.org/10.26599/NRE.2023.9120070.

[10] D.G. Zheng, H.D. Lee, G.W. Lee, D.S. Shin, J.W. Kim, J.I. Shim, Z.Q. Lin, T.W. Lee, D.H. Kim, Investigation into charge carrier dynamics in organic light-emitting diodes, Nano Res. Energy 3 (2024) e9120129, https://doi.org/10.26599/NRE.2024.9120109.

[11] J. Wang, W. Cui, Q. Liu, Z. Xing, A.M. Asiri, X. Sun, Recent progress in cobaltbased heterogeneous catalysts for electrochemical water splitting, Adv. Mater. 28 (2016) 215–230, https://doi.org/10.1002/adma.201502696.

[12] J. Tian, Q. Liu, A.M. Asiri, X. Sun, Self-supported nanoporous cobalt phosphide nanowire arrays: an efficient 3D hydrogen-evolving cathode over the wide range of pH 0-14, J. Am. Chem. Soc. 136 (2014) 7587–7590, https://doi.org/10.1021/ja503372r.

[13] Y. Lee, J. Suntivich, K.J. May, E.E. Perry, Y. Shao-Horn, Synthesis and activities of rutile IrO_2 and RuO_2 nanoparticles for oxygen evolution in acid and alkaline solutions, J. Phys. Chem. Lett. 3 (2012) 399–404, https://doi.org/10.1021/jz2016507.

[14] J.B. Gerken, J.G. McAlpin, J.Y.C. Chen, M.L. Rigsby, W.H. Casey, R.D. Britt, S. S. Stahl, Electrochemical water oxidation with cobalt-based electrocatalysts from pH 0-14: the thermodynamic basis for catalyst structure, stability, and activity, J. Am. Chem. Soc. 133 (2011) 14431–14442, https://doi.org/10.1021/ja205647m.

[15] J. Rosen, G.S. Hutchings, F. Jiao, Ordered mesoporous cobalt oxide as highly efficient oxygen evolution catalyst, J. Am. Chem. Soc. 135 (2013) 4516–4521, https://doi.org/10.1021/ja400555q.

[16] H.R. Ren, Z.K. Zhang, S.L. Xu, K. Jia, H.Y. Zhou, R.D. Zhao, D.P. Zhao, M.G. Li, Design and fabrication of high-performance $ZnCo_2O_4/ZnWS_4$ composite electrode materials for advanced asymmetric supercapacitors, Ionics 31 (2025) 8511–8524, https://doi.org/10.1007/s11581-025-06379-x.

[17] B.Y. Zhang, S.L. Xu, J. Li, X.X. Zhao, R.D. Zhao, M.C. Zhang, D.P. Zhao, L.H. Miao, Ruthenium-modified oxygen-deficient NiCoP catalysts for efficient electrocatalytic water splitting, CrystEngComm 27 (2025) 5485, https://doi.org/10.1039/D5CE00510H.

[18] P. Chen, K. Xu, Z. Fang, Y. Tong, J. Wu, X. Lu, X. Peng, H. Ding, C. Wu, Y. Xie, Metallic Co_4N porous nanowire arrays activated by surface oxidation as electrocatalysts for the oxygen evolution reaction, Angew, Chem. Int. Ed. 127 (2015) 14923–14927, https://doi.org/10.1002/ange.201506480.

[19] Y. Zhang, B. Ouyang, J. Xu, G. Jia, S. Chen, R.S. Rawat, H.J. Fan, Rapid synthesis of cobalt nitride nanowires: highly efficient and low-cost catalysts for oxygen evolution, Angew. Chem. Int. Ed. 128 (2016) 8812–8816, https://doi.org/10.1002/ange.201604372.

[20] H.Y. Zhou, Z.K. Zhang, Q.H. Zhang, B.Y. Zhang, X. Li, S.L. Xu, R.D. Zhao, X. M. Zhao, D.P. Zhao, M.G. Li, F.F. Wu, Multidimensional engineering strategies for transition metal selenide electrocatalysts in water electrolysis with performance optimization mechanisms and future perspectives, Chem. Rec. 8 (2025) e2500082, https://doi.org/10.1002/tcr.202500082.

[21] D. Kong, J.J. Cha, H. Wang, H.R. Lee, Y. Cui, First-row transition metal dichalcogenide catalysts for hydrogen evolution reaction, Energy Environ. Sci. 6 (2013) 3553–3558, https://doi.org/10.1039/C3EE42413H.

[22] Y.Q. Tian, S.L. Xu, J. Li, S.S. Zhang, B.Y. Zhang, R.D. Zhao, F.F. Wu, D.P. Zhao, Vanadium-cobalt oxide nanoflower catalyst for efficient and stable overall water splitting in alkaline and seawater electrolytes, Research 2 (2025) 100647, https://doi.org/10.1016/j.nexres.2025.100647.

[23] C. Bai, S. Wei, D. Deng, X. Lin, M. Zheng, Q. Dong, A nitrogen-doped nano carbon dodecahedron with $Co@Co_3O_4$ implants as a bi-functional electrocatalyst for efficient overall water splitting, J. Mater. Chem. A 5 (2017) 9533–9536, https://doi.org/10.1039/C7TA01708A.

[24] M. Guo, Y. Liu, S. Dong, X. Jiao, T. Wang, D. Chen, Co9S8-catalyzed growth of thin-walled graphite microtubes for robust, efficient overall water splitting, ChemSusChem 11 (2018) 4150–4155, https://doi.org/10.1002/cssc.201802055.

[25] X. Chen, X. Zhen, H. Gong, L. Li, J. Xiao, Z. Xu, D. Yan, G. Xiao, R. Yang, Cobalt and nitrogen codoped porous carbon as superior bifunctional electrocatalyst for oxygen reduction and hydrogen evolution reaction in alkaline medium, Chin. Chem. Lett. 30 (2019) 681–685, https://doi.org/10.1016/j.cclet.2018.09.017.

[26] C.N. Lv, L. Zhang, X.H. Huang, Y.X. Zhu, X. Zhang, J.S. Hu, S.Y. Lu, Double functionalization of N-doped carbon carved hollow nanocubes with mixed metal phosphides as efficient bifunctional catalysts for electrochemical overall water splitting, Nano Energy 65 (2019) 103995, https://doi.org/10.1016/j.nanoen.2019.103995.

[27] Y. Lin, Y. Pan, S. Liu, K. Sun, Y. Cheng, M. Liu, Z. Wang, X. Li, J. Zhang, Construction of multi-dimensional core/shell Ni/NiCoP nano-heterojunction for efficient electrocatalytic water splitting, Appl. Catal., B 259 (2019) 118039, https://doi.org/10.1016/j.apcatb.2019.118039.

[28] S.S. Zhang, R.Y. Li, X. Li, Y.Q. Tian, R.D. Zhao, J. Xiang, F.F. Wu, R.D. Zhao, Hydrothermally synthesized NiSe2 nanospheres for efficient bifunctional electrocatalysis in alkaline seawater electrolysis: high performance and stability in HER and OER, Mater. Res. Bull. 189 (2025) 113463, https://doi.org/10.1016/j.materresbull.2025.113463.

[29] Y.W. Wu, X.Q. Du, X.S. Zhang, P doping transition metal sulfides as bifunctional electrocatalyst for overall seawater splitting, Int. J. Hydrogen Energy 103 (2025) 174–182, https://doi.org/10.1016/j.ijhydene.2025.01.181.

[30] Y.M. Wang, L.L. Chen, H.M. Zhang, M. Humayun, J.H. Duan, X.F. Xu, Y.J. Fu, M. Bououdina, C.D. Wang, Elaborately tailored NiCo2O4 for highly efficient overall water splitting and urea electrolysis, Green Chem. 25 (2023) 8181–8195, https://doi.org/10.1039/d3gc01828h.

[31] L.C. Yao, H.M. Zhang, M. Humayun, Y.J. Fu, X.F. Xu, C.D. Feng, C.D. Wang, Constructing nanoporous crystalline/amorphous NiFe2O4/NiO electrocatalyst for high efficiency OER/UOR, J. Alloys Compd. 936 (2023) 168206. https://doi-org.ezproxy.its.uu.se/10.1016/j.jallcom.2022.168206.

[32] X. Li, S.l. Xu, J. Li, S.S. Zhang, B.Y. Zhang, R.D. Zhao, D.P. Zhao, F.F. Wu, NiFe-LDH as a bifunctional electrocatalyst for efficient water and seawater electrolysis:

enhanced oxygen evolution and hydrogen evolution reactions, Nanoscale Adv. 7 (2025) 5546–5560, https://doi.org/10.1039/D5NA00350D.
[33] B.J. Chen, M. Humayun, Y.D. Li, H.M. Zhang, H.C. Sun, Y. Wu, C.D. Wang, Constructing hierarchical fluffy CoO−Co_4N@NiFe-LDH nanorod arrays for highly effective overall water splitting and urea electrolysis, ACS Sustainable Chem. Eng. 9 (2021) 14180–14192, https://doi.org/10.1021/acssuschemeng.1c04674.
[34] Z.h. Huang, J. Zhang, M. Humayun, Y.X. Liu, W.B. Xiao, C.D. Feng, K. Zhao, B. Wu, Y.J. Fu, M. Bououdina, H.M. Zhang, G.X.J. Chen, C.D. Wang, Molybdenum-leveraged mott-schottky heterojunction for advanced water splitting and urea electrolysis, J. Energy Chem. 111 (2025) 94–108. https://doi-org.ezproxy.its.uu.se/10.1016/j.jechem.2025.07.044.
[35] J.L. Chang, F.F. Song, F. Xu, D.P. Wu, Y. Hou, K. Jiang, Y.M. Guo, Z.Y. Gao, Enhanced electrocatalytic efficiencies for water electrolysis and *para*-nitrophenol hydrogenation by self-supported nickel cobalt phosphide-nickel iron layered double hydroxide p-n junction, J. Colloid Interface Sci. 653 (2024) 1063–1074, https://doi.org/10.1016/j.jcis.2023.09.156.
[36] S.Q. Zang, Y. Hou, J.L. Chang, F. Xu, D.P. Wu, K. Jiang, Z.Y. Gao, Amorphous-crystalline heterostructures enable energy-level matching of cobalt sulfide/nickel iron layered double hydroxide for efficient oxygen evolution reaction, J. Colloid Interface Sci. 656 (2024) 485–494, https://doi.org/10.1016/j.jcis.2023.11.124.
[37] H.Y. Jin, J. Xu, H. Liu, H.F. Shen, H.M. Yu, M. Jaroniec, Y. Zheng, S.Z. Qiao, Emerging materials and technologies for electrocatalytic seawater splitting, Sci. Adv. 9 (2023), https://doi.org/10.1126/sciadv.adi7755 eadi7755.
[38] Z.B. Zhai, K.J. Huang, X. Wu, Superior mixed Co-Cd selenide nanorods for high performance alkaline battery-supercapacitor hybrid energy storage, Nano Energy 47 (2018) 89–95, https://doi.org/10.1016/j.nanoen.2018.02.059.
[39] H.Y. Zhou, R.Y. Li, S.L. Xu, B.Y. Zhang, R.D. Zhao, X.M. Zhao, F.F. Wu, D.P. Zhao, Interface engineering induced homogeneous isomeric bimetallic of CoSe/$NiSe_2$ electrocatalysts for high performance water/seawater splitting, Adv. Sustain. Syst. 9 (2025) 2400849, https://doi.org/10.1002/adsu.202400849.
[40] S. Prabu, G. Nagaraju, S. Sengodan, K.Y. Chiang, Highly stable bifunctional heterostructured electrocatalyst integrated with LDPE-derived spherical carbon for longevous alkaline seawater splitting, Small 21 (2025) 2500453, https://doi.org/10.1002/smll.202500453.
[41] Y.W. Wu, X.Q. Du, X.S. Zhan, Fe-doped CoMoO/Ni S grown on Ni foam as a multifunctional electrode for electrocatalytic seawater and urea splitting, J. Alloys Compd. 1030 (2025) 180927. https://doi-org.ezproxy.its.uu.se/10.1016/j.jallcom.2025.180927.
[42] Y.H. Wang S, J. Liu, X.Q. Du, X.S. Zhang, Controlled synthesis of Co–Ni_3Se_2/MoS_2/Ni_3S_2 nanoarrays as robust electrocatalyst for urea and seawater oxidation reaction, Int. J. Hydrogen Energy 88 (2024) 450, https://doi.org/10.1016/j.ijhydene.2024.09.222.
[43] R.Y. Li, X.Y. Shen, J. Li, D.P. Zhao, R.D. Zhao, F.F. Wu, Enhanced electrochemical performance of NiCo-Layered double hydroxides: optimal synthesis conditions and supercapacitor applications, Adv. Sustain. Syst. 9 (2025) 2400753, https://doi.org/10.1002/adsu.202400753.
[44] C. Li, Z.J. Zhang, R. Liu, In situ growth of 3D NiFe LDH-POM micro-flowers on nickel foam for overall water splitting, Small 16 (2020) 2003777, https://doi.org/10.1002/smll.202003777.
[45] Z. Yang, Y. Lin, F.X. Jiao, J.H. Li, J.L. Wang, Y.Q. Gong, In situ growth of 3D walnut-like nano-architecture Mo-Ni_2P@NiFe LDH/NF arrays for synergistically enhanced overall water splitting, J. Energy Chem. 49 (2020) 189–197, https://doi.org/10.1016/j.jechem.2020.02.025.
[46] S. Dutta, A. Indra, Y. Feng, T. Song, U. Paik, Self-supported nickel iron layered double hydroxide-nickel selenide electrocatalyst for superior water splitting activity, ACS Appl. Mater. Interfaces 9 (2017) 33766–33774, https://doi.org/10.1021/acsami.7b07984.
[47] F.X. Yang, M.R. Mu, K.Q. Zhang, Ultralong NiSe nanowire anchored on graphene nanosheets for enhanced electrocatalytic performance of triiodide reduction, RSC Adv. 11 (2021) 27681–27688, https://doi.org/10.1039/d1ra04367f.
[48] W.T. Wu, B.Y. Min, H.B. Li, F. Liu, M.S. Zheng, K.P. Ding, S.J. Lu, M.C. Liu, NiFe-LDH coated NiSe/Ni foam as a bifunctional electrocatalyst for overall water splitting, React. Chem. Eng. 8 (2023) 1711–1718, https://doi.org/10.1039/D3RE00004D.
[49] M.R. Pallavolu, S. Prabu, J.S. Al-Otaibi, S. Pandiaraj, G. Koyyada, T.V. M. Sreekanth, Integrated NiOOH@CoMnS hierarchical nanostructured electrocatalyst for sustainable hydrogen conversion via alkaline seawater electrolysis: synergistic design and mechanistic insights, J. Mater. Chem. A 13 (2025) 29218, https://doi.org/10.1039/D5TA04643B.
[50] S.C. Karthikeyan, R.S. Kumar, S. Ramakrishnan, S. Prabhakaran, A.R. Kim, D. H. Kim, D.J. Yoo, Efficient alkaline water/seawater electrolysis by development of ultra-low IrO_2 nanoparticles decorated on hierarchical MnO_2/rGO nanostructure, ACS Sustainable Chem. Eng. 10 (2022) 15068–15081, https://doi.org/10.1021/acssuschemeng.2c04074.